Gradient Coil Design and Construction for a Halbach Based MRI System

B. de Vos

Technische Universiteit Delft

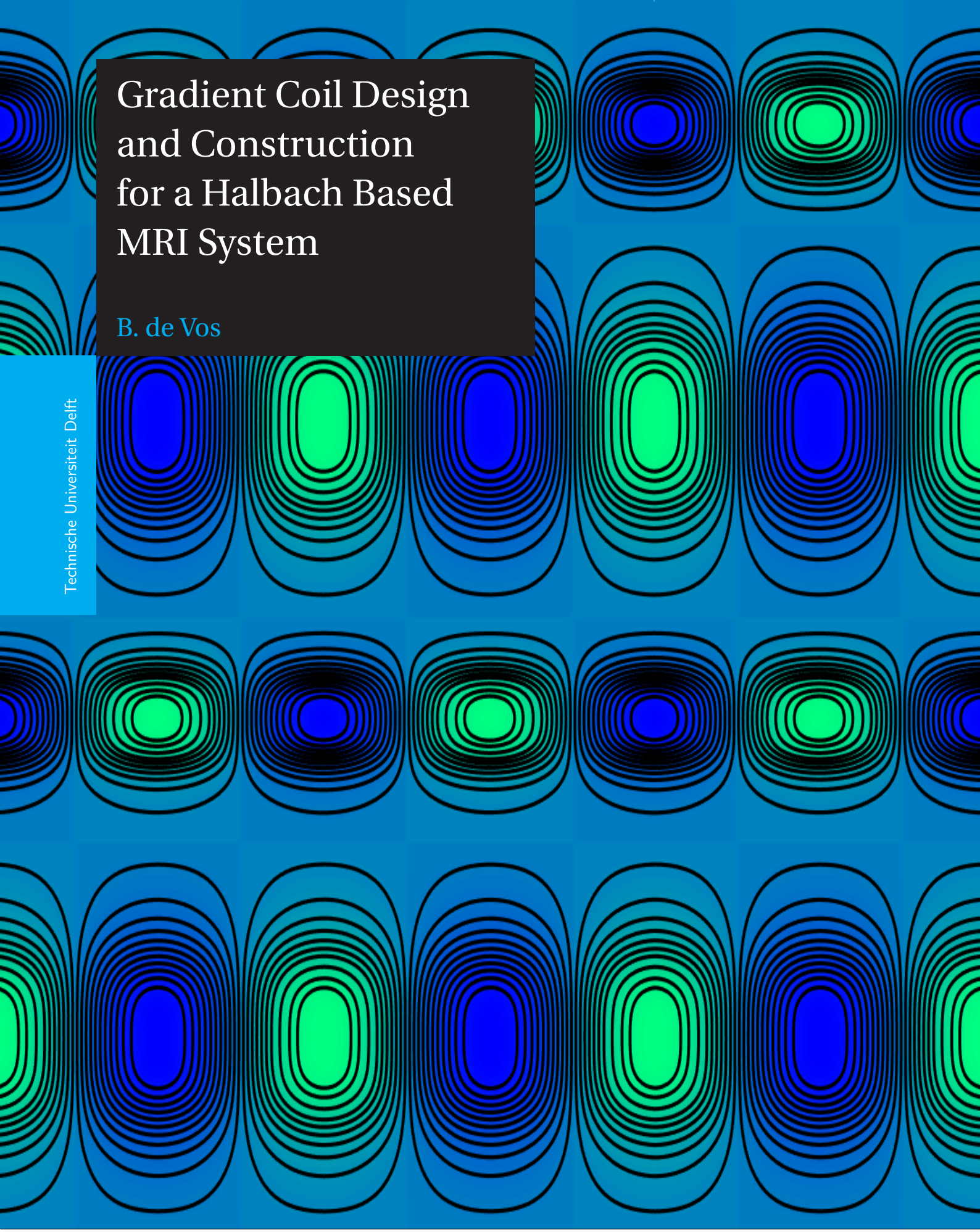

TU Delft Delft University of Technology

Challenge the future

Gradient Coil Design and Construction for a Halbach Based MRI System

by

B. de Vos

in partial fulfillment of the requirements for the degree of

Master of Science
in Electrical Engineering

at the Delft University of Technology,

to be defended publicly on Wednesday June 26, 2019 at 10:00 AM

Student number:	4180038
Project duration:	November 19, 2018 - June 26, 2019
Thesis committee:	Dr. R.F. Remis, Prof. A.G. Webb, Dr. M.B. van Gijzen, Ir. P.S. Fuchs.

ABSTRACT

MRI as a medical diagnostics tool is still unavailable to the majority of the developing world. Therefore the design and development of new low-cost hardware are essential. The design of gradient coils corresponding to this hardware is necessary for conventional imaging and reconstruction methods to be used.

The target field method, which was originally developed to deal with longitudinal main magnetic fields, is applied to a transverse field, as produced by a Halbach permanent magnet array. Using this method current densities for gradient fields in the three spatial directions are derived. Subsequently, using stream functions, wire patterns for the three gradient coils are determined. These are verified using a commercial magnetostatic solver. Furthermore, one of the gradients is constructed to validate the performance of the method.

The measured fields are in good agreement with the simulations and their prescribed target fields. This confirms that the proposed method provides a reliable way to design and manufacture gradient coils for various requirements. Based on the experimental review of the constructed coil three optimized gradients are proposed for the low field MRI system developed at the LUMC in cooperation with the TU Delft. The method can also be readily generalized to other geometries and requirements due to the robust fundamental physical basis and accuracy with respect to computer simulations.

ACKNOWLEDGEMENTS

The origin of my work can be traced back to 2011 when I first met Rob Remis during a first year group project. Rob was our supervisor and I remember him being helpful and patient. We got along quite well and I liked how we could have a laugh while being formal when needed. Halfway through my masters I approached Rob to talk about possible thesis subjects and course choices. This was when I first heard about the low field project. It immediately caught my attention, the medical aspect in combination with it being a group project seemed perfect to me. I was happy to hear that the courses I had in mind coincided with the required background.

Getting the responsibility of designing the gradient coils was more then I could wish for. The theoretical work combined with the possibility of actually building a prototype is something that is not easy to find. I remember talking to Rob about the academic level and that we should be wary that it would not get to practical. I think it is safe to say that in the end we got what we wanted.

Throughout the process Rob was a great supervisor. I always felt like he was there when I needed him, despite his busy schedule. He was very committed to the project and put a lot of time and effort into helping me with my work. I want to thank Rob for his support and all the fun times we had in the past months.

My daily supervisor Patrick Fuchs was also indispensable. He gave me great insights and was a key player in the beginning of the project when I needed extra guidance. His notes on my written work were essential for the final product and he always made time for me. He never ceases to amaze me with his trivia knowledge and the endless conversations I can have with him.

The Gorter team was the group that made the project come to life. I made a lot of friends in Leiden and I loved how I could ask anyone for help. I want to express my gratitude to Andrew Webb for giving me the opportunity of working on the gradient coils. He gave me the freedom of working on it with my own vision. Furthermore, I want to thank Tom O'Reilly he is essential for the low field project. I respect his work ethic, his patience and great sense of humor. He was my partner in crime and gave me great ideas on how to improve my work. I also would like to express my gratitude to Wouter Teeuwisse. I was always told by my parents that I have two left hands but I am not sure that this still applies. Wouter taught me how to actually realize a design and he has given me great tips with respect to the construction of the gradient coil. Wouter is a safety guru and without him I would have electrocuted myself at least once. Lastly I want to thank my office friends in Leiden for their cynical sense of humor and pulling me through the rougher patches of this project.

I want to thank Martin van Gijzen and Andrew Webb for taking the time to be on my committee and reading my thesis.

During this work my family and friends have given me the distraction I sometimes needed, for this I am grateful. I also want to thank my girlfriend Danique. Her infinite patience with me is inspiring. She respected the time I wanted to put into the project and my best ideas and breakthroughs occurred when I was with her.

I wish everyone involved in the low field project the best of luck and I am certain that the scanner will grow out to become a major success.

Bart de Vos
Delft, The Netherlands
4th of June 2019

CONTENTS

1 INTRODUCTION

Hydrocephalus is a disease that is frequently encountered in sub-Saharan Africa. More than 200.000 infants suffer from this disease every year [1]. The disease causes buildup of excess cerebrospinal fluid (CSF) inside the brain, which can be fatal if left untreated. The fluid will normally flow free around the brain and through its ventricles. With hydrocephalus the CSF is not absorbed in the bloodstream and builds up inside the brain. In order to treat hydrocephalus a shunt can be surgically placed which drains the excess fluid [2]. Placing these shunts requires knowledge of the location and severity of the fluid buildup which is acquired through imaging or surgery. Common non-invasive procedures for imaging the brain are computed tomography (CT), magnetic resonance imaging (MRI) and ultrasound. CT and MRI are expensive techniques and both are not widely available in Africa [3]. Ultrasound is an inexpensive alternative but can only be used up to about 6 months after birth when the skull bone has not completely fused.

At this moment CT is the standard for imaging hydrocephalus in developing countries. After shunt placement a child needs multiple followup scans, which results in a radiation burden. MRI scans do not utilize ionizing radiation and are therefore associated with less risk. Moreover, a low resolution scan could be sufficient in order to obtain the information required for diagnosis and shunt placement. This is illustrated in Figure 1.1 which shows an MRI image of a diseased and a healthy brain. The dark tissue inside the brain in the left part of the figure represents the excess fluid.

MRI is a technique designed in and for the developed world. The technique is moving towards more detailed and specific images and is getting more expensive. There is however a certain urgency for an affordable robust solution in developing countries. In November 2017 an open source project to develop a low cost MRI scanner (<50.000$) was therefor initiated. The system is meant for the diagnosis and treatment of the above mentioned condition. It also needs to work in the environment of a developing country like Uganda. This means that the device and its components should preferably be low maintenance, robust and portable.

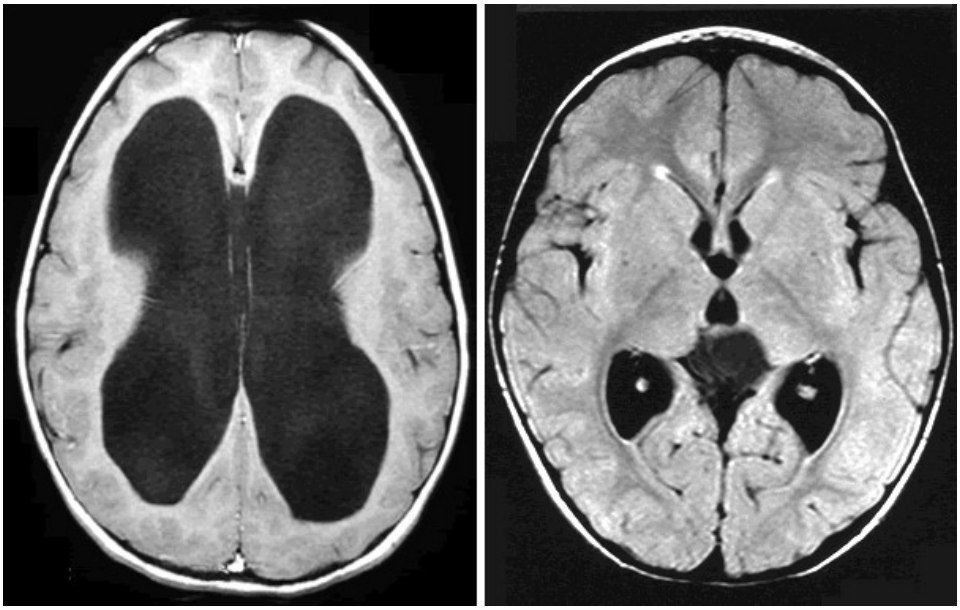

Figure 1.1: Two MRI brain scans. One brain with hydrocephalus (left) and one healthy brain (right). The dark area inside the brain on the left scan show the enlarged ventricles containing CSF build up [4].

The project is split up into two different designs with the same goal. One is being developed at the Leiden University Medical Center (LUMC) in close collaboration with the Technical University Delft (TUD). The other is being developed by the Pennsylvania State University (Penn State) in the USA. In addition the project also has partners in Uganda where the system will eventually be used. The primary difference between the two systems is the magnet design. In conventional MRI the main magnetic field is very strong. This is due to the signal to noise ratio (SNR) being proportional to the magnetic field strength. This strong field is generated with superconducting coils. The superconductivity is obtained by cooling the coils to extremely low temperatures using liquid helium. This makes the system very expensive. Both Penn State and the LUMC remove these super conducting coils resulting in a low field MRI system. Penn State uses resistive coils to generate the main magnetic field. The version developed in the Netherlands uses permanent magnets. In addition to the magnet, all other MRI components are redesigned in order to fulfill the low cost requirement and work with the nonstandard magnetic field. This work will focus on the gradient coils.

Gradient coils are a vital component in MRI. They create the spatial encoding which is essential for image reconstruction. Gradient coils can be thought of as very low frequency antennas. They work in the near field and create desired perturbations in the main magnetic field. Designing gradient coils for the low field system brings a number of challenges:

- The gradient field direction should correspond to the direction of the main magnetic field. The permanent magnet design of the LUMC system has a different magnetic field direction with respect to a conventional MRI.
- The coils need to operate at low power in order to be deployed in a low resource infrastructure. Also the heating of the coils is undesired as this will influence the permanent magnets.
- The dimensions of the gradient coils need to be relatively small to fit inside the low field system.
- The total cost of the gradient coils need to be kept as low as possible. Furthermore, it would be preferable if these coils can be built locally.

These challenges require us to reinvent the gradient coil for the purpose of this system. This work contains all the steps from deriving the equations meant for designing a gradient coil to the construction and testing of the coil. In the remaining part of this chapter we give background information on gradient coil designs and end with an overview of the system. In Chapter 2 we derive the equations that form the backbone of this thesis. The derivation starts from first principles and ends with one equation describing each gradient coil. In Chapter 3 we implement the equations and verify their working. In addition, the performance of the resulting gradient coils is examined. A gradient coil producing a linear field along the bore of the axis is then designed specifically for the low field system. This coil is also built and tested. The end of this chapter holds the recommended designs for all these low field gradient coils. The conclusions and recommendations of the total work can be found in Chapter 4.

1.1. GRADIENT FIELDS IN MRI

The spatial encoding required to obtain information on where the signal in space originated from is created by the gradient fields. These fields create a change in resonance frequency of hydrogen protons in the human body. This resonance frequency is proportional to the magnetic flux density and is given by

$$f = \gamma B. \tag{1.1}$$

The gyromagnetic ratio γ is a nuclei specific constant. We can obtain frequency encoding by creating known perturbations in the main magnetic field (B_0). These variations are usually small in terms of the main magnetic field strength and are chosen to vary linearly with position. Hence the name *gradient* fields. Linear fields are chosen in order to use the Fourier transform during the reconstruction process [5]. These fields are created in three orthogonal directions in order to distinguish a point unambiguously in space. Each direction has its own gradient coil which can be controlled independently. The fields generated by the gradient coils all point in the B_0 direction and vary in strength in the Cartesian x,y or z direction.

Creating a gradient field solely in the direction of the main magnetic field is not possible. The Maxwell equations state that additional components called concomitant fields are also created. In general these components can be ignored if the they are small compared with the main magnetic field [6],[7]. In this work the

concomitant field values were not found significant. More background information on the physics and sequences of MRI can be found in [8]. Information on MRI systems and components can be found in [9].

In gradient coil design we want to obtain linear varying fields with a certain field strength inside the volume of interest (VOI). This while minimizing the power dissipation and inductance. This is easier said than done as some of these parameters are conflicting with each other. In the next part these design parameters and their importance to the low field system will be discussed.

The current supplied to the gradient coils is directly proportional to the gradient field strength which can be written as

$$G = \eta I \tag{1.2}$$

Values of the gradient strength are often in the regions of 10mT/m. The gradient field strengths need to be chosen high enough to overcome the unknown inhomogeneities of the main magnetic field. The parameter η (T/m/A) is the efficiency of the gradient coil. This is the amount of field generated with 1A of current. The required current is also inversely proportional to the amount of turns. As the spreading of the field is proportional to r^2, the required current also varies in the same manner.

The inductance of the coil is influenced by the amount of turns and the concentration of current density. This influences the rise time of the gradient coils. If the inductance becomes larger more energy is stored, consequently it takes longer for the gradient coils to reach their desired field value. Having a low inductance is important when sequences are used that require fast switching gradients. The inductance is proportional to r^5 [10].

The power dissipation of the gradient coils is equal to $P = I^2R$. The resistance of the coil can be influenced by the amount of turns as well as the size and the type of conductor. The resistance can be assumed to be proportional to the radius of the coil. This makes the power dissipation proportional to r^5. In conventional coil designs driving currents of more than a hundred ampere are quite common. In order to deal with the resulting heating large water cooled conductors are often used to synthesize the gradient coils.

The low field system primarily uses spin echo sequences which do not require fast switching gradients. Having a low inductance is thus of less importance in comparison with conventional MRI. Power dissipation is our main concern. It is needless to say that large complex water-cooled gradient coils are undesired for an MRI system that is meant for a low resource setting. Furthermore, the fields that the permanent magnets exert are temperature dependent. Heating of these magnets can influence the image quality and even damage the system. Keeping the current low is thus our main concern. The relatively small bore size of the low field system helps our low power requirement. Moreover, the imaging volume is smaller than with conventional MRI as we are primarily interested in imaging the head.

Gradient coils can be designed in various ways. Methods using discrete and distributed windings can be distinguished. With the first, winding positioning is used to remove higher order terms in the Taylor series. Canceling specific terms will lead to a linear field. These are simple but effective methods which have given reasonable coil designs. With these methods accurate position of the turns is crucial. Furthermore, the performance when deviating from the central line has been found to be poor. With distributed winding methods turns are placed to approximate a continuous current density. These methods yield coils with a better gradient efficiency, more design freedom and a lower inductance due to the current density being more spread out. This current density can be obtained in various ways. The most popular approach is the target field method proposed by Turner [11]. This method gives more physical insight with respect to other design approaches. The computation time is short because Fourier analysis of simple structures like a cylinder or plane is used. Furthermore, the target field method has extensions which are used often in state of the art gradient coils. Minimum inductance [12], minimum power [13] and constrained length [14] are mostly used. The target field method will be adopted in this work. More information on the alternative design methods can be found in the review papers [15],[16].

1.2. SYSTEM OVERVIEW

The Halbach array which creates the main magnetic field is shown in Figure 1.2. The figure shows the coordinate system adopted in this work. The magnetic field is created by positioning small magnets in a Halbach orientation. The superposition of these magnets creates a near homogeneous field in the direction perpendicular to the bore. This direction corresponds with the x-direction. This means the gradient fields need to have their magnetic field oriented in this direction. The magnet creates a central field strength of 50.54mT. We want to image in a 20cm diameter of spherical volume (DSV) [17]. The gradient coils need to fit inside the low field magnet system. We want to place the gradient coils as close as possible to the imaging domain. Figure 1.3 shows a cross section view of the magnet. The blue square denotes where the shim coils of the low field magnet are located. The red square shows a section of 20x370mm where the gradient coils can be placed. The RF-coil can fit inside the 270mm bore which leaves approximately 250mm of space for imaging.

The gradient coils should fit in the cavity mentioned above and will be designed to a maximum length of 350mm leaving room for the connecting wires and ports. The required field strength is set at 10mT/m. The region where spatial encoding can be applied is required to be 200x200x150mm (x,y,z). The gradient coils should not heat up the magnets while running imaging sequences.

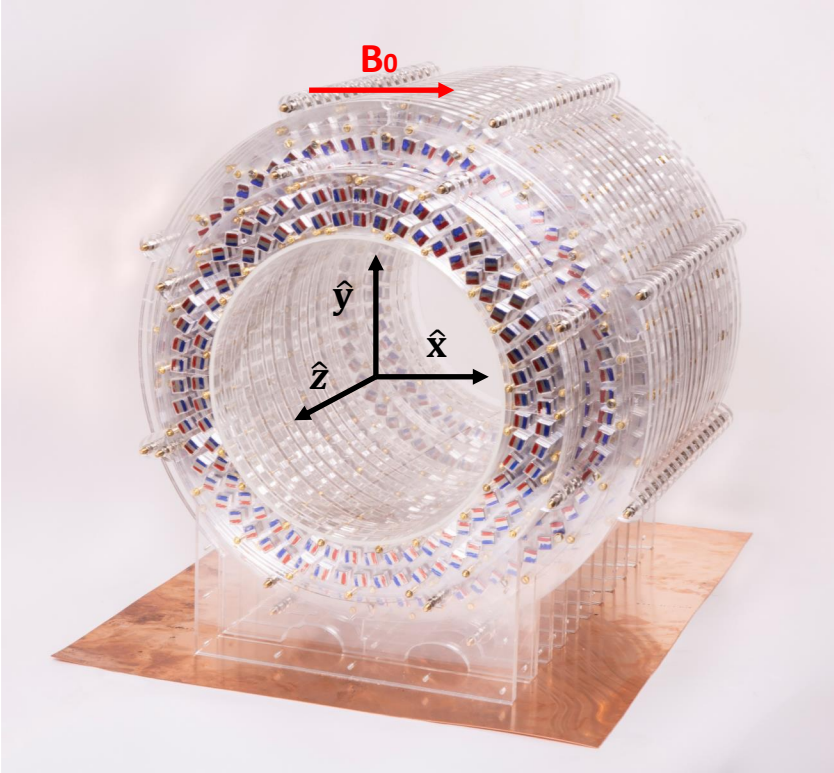

Figure 1.2: The low field magnet system. The system consists of 2948 permanent magnets in a Halbach configuration. The direction of the main magnetic field B_0 is shown with an arrow and is transverse to the bore. Courtesy of T. O'Reilly (LUMC)

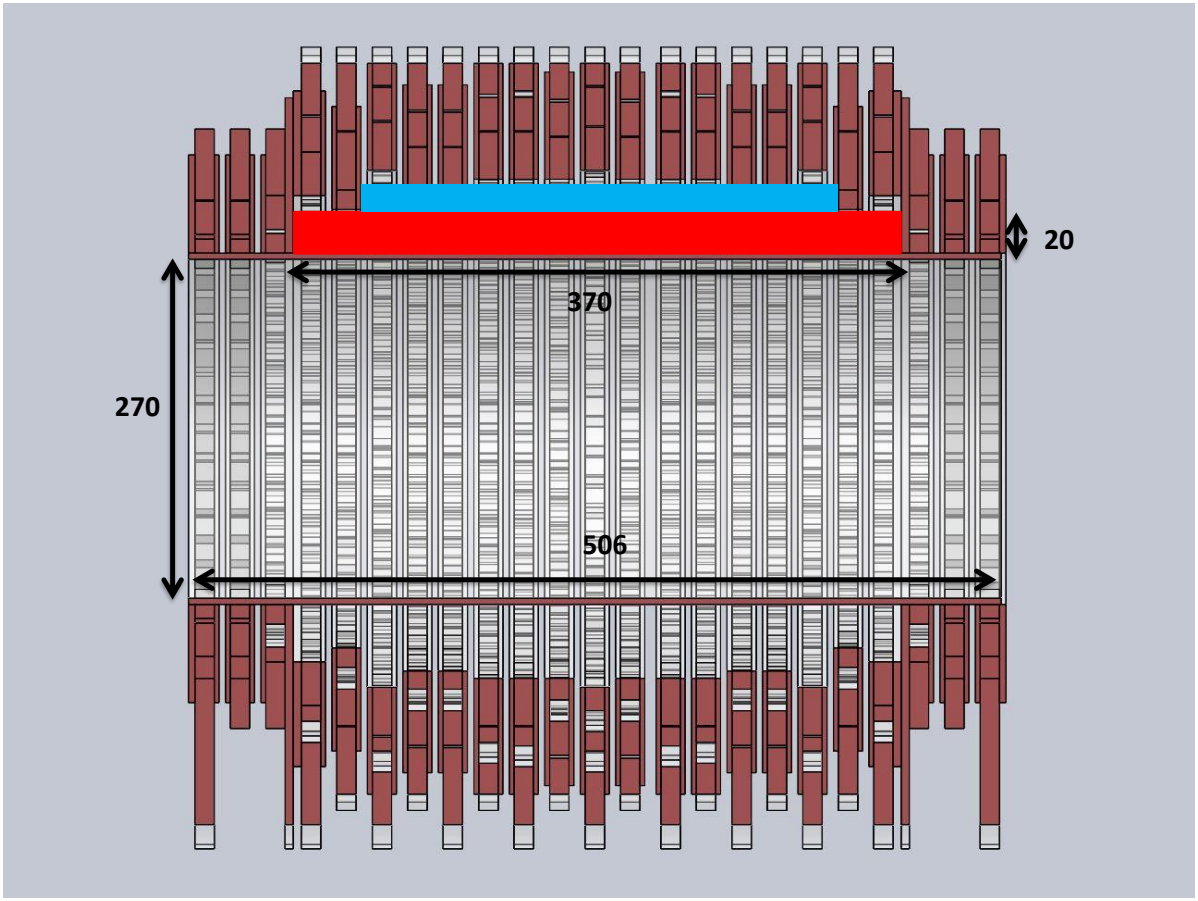

Figure 1.3: Cross section of the low field magnet, the blue rectangle indicates the space where the shim coils are positioned. The red region shows where the gradient coils can be placed this is a region of 370x20mm. All dimensions in the figure are in millimeters. Courtesy of T. O'Reilly (LUMC)

2

GRADIENT COIL DESIGN: THE TARGET FIELD APPROACH

The target field field approach is a powerful and versatile method used in gradient coil design. It was first proposed by Robert Turner in 1985 [11]. The method describes a relationship between a desired gradient field and a surface current density that generates it. The obtained current density can be approximated by current carrying tracks or wires resulting in a gradient coil.

The target field approach is an inverse source problem. The source corresponding to a prescribed field needs to be found. This problem type is generally ill-posed. This means that there can be many solutions, the solutions can be unstable or there are no solutions at all. What makes the target field approach so powerful is that a solution results in single equation for each coil. This is realized by exploiting cylindrical symmetry, Fourier analysis, and properly selecting the target fields.

The original approach proposed by Turner is meant for conventional MRI. The derivation is carried out in cylindrical coordinates and the target field component is taken along the bore. In this work, however, we are interested in a Halbach setup and the magnetic field component that is *perpendicular* to the bore is of interest. This component is composed of two cylindrical components and, consequently, the present target field analysis will run along different lines compared with the standard approach that is followed for a magnetic field component that is directed along the bore axis.

In Section 2.1 we present the basic magnetic field equations and derive the basic relations between the various magnetic field components and the surface current densities that generate this field. Subsequently, we describe the desired target fields in Section 2.2. How to realize surface current densities that produce these desired fields is discussed in Section 2.3 and converting these current densities into current paths using stream function theory is discussed in Section 2.4.

2.1. DERIVATION RELATIONSHIP TARGET FIELDS AND CURRENT DENSITY

The target field equations will be derived for the configuration shown in Figure 2.1. The figure shows a cross section of an infinitely long cylinder extended in the z-direction. Two regions can be distinguished: region I inside the cylinder with radius a and region II outside this cylinder. The surface current density $\boldsymbol{J_s}(a,\phi,z)$ that produces the field is confined to the surface of the cylinder. The goal of this section is to find a relationship between the magnetic flux density and the surface current that produces it. There are no sources present in region I and II as these are confined to the surface. In addition, time variations of the gradient coils and fields allow us to restrict ourselves to the basic magnetostatic field equations

$$\nabla \cdot \mathbf{B} = 0, \tag{2.1}$$

$$\nabla \times \mathbf{B} = 0. \tag{2.2}$$

Clearly, the magnetic flux density is divergence and curl free in regions I and II. The first equation is automatically satisfied if we write the magnetic flux density as the curl of a vector potential $\mathbf{A}$, while the second equation is automatically satisfied if we write the magnetic flux density as the gradient of a scalar potential Φ. Both approaches can be followed, of course. Here we consider the second approach and write the flux density as

$$\mathbf{B} = -\nabla\Phi. \tag{2.3}$$

The function Φ is the scalar magnetic potential and is expressed in Vs/m. Substituting Equation 2.3 into 2.1 results in Laplace's equation for the potential

$$\nabla^2\Phi = 0, \tag{2.4}$$

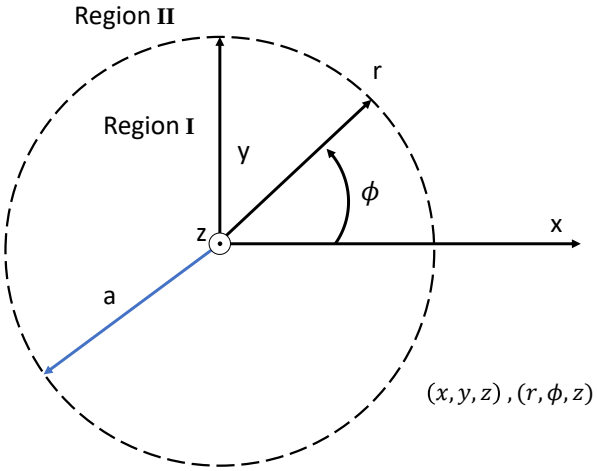

Figure 2.1: The configuration used to derive the target field equations

which holds in region I and in region II. Given the cylindrical structure of our configuration, it is advantageous to write Equation 2.4 in cylindrical coordinates. We have

$$\frac{\partial^2\Phi}{\partial r^2} + \frac{1}{r}\frac{\partial\Phi}{\partial r} + \frac{1}{r^2}\frac{\partial^2\Phi}{\partial\phi^2} + \frac{\partial^2\Phi}{\partial z^2} = 0. \tag{2.5}$$

Moreover, the infinite length of the cylinder makes the configuration invariant in the z-direction and the fields must be 2π-periodic in the ϕ-direction as well. We can take advantage of these two geometrical properties by introducing a two-dimensional Fourier transform

$$\tilde{\Phi}^m(r,k) = \int_{z=-\infty}^{\infty}\int_{\phi=-\pi}^{\pi} \Phi(r,\phi,z)e^{-jm\phi}e^{-jkz}\mathrm{d}z\mathrm{d}\phi, \tag{2.6}$$

with $k \in \mathbb{R}$ and $m \in \mathbb{Z}$ labels the discrete angular Fourier modes. The inverse Fourier transform that corresponds to the above forward transform is given by

$$\Phi(r,\phi,z) = \frac{1}{4\pi^2}\int_{k=-\infty}^{\infty}\sum_{m=-\infty}^{\infty}\tilde{\Phi}^m(r,k)e^{jm\phi}e^{jkz}\mathrm{d}k. \tag{2.7}$$

It is easy to verify that the Fourier transform is linear and the transform has the following properties with respect to differentiation

$$\frac{\partial}{\partial\phi} \overset{\mathfrak{F}}{\longleftrightarrow} jm, \tag{2.8}$$

$$\frac{\partial}{\partial z} \overset{\mathfrak{F}}{\longleftrightarrow} jk. \tag{2.9}$$

Another important property that will be used later on is the modulation property. Multiplying by $e^{jn\phi}$, with n an integer, corresponds to an angular modulation, which transforms into

$$\Phi(r,\phi,z)e^{jn\phi} \overset{\mathfrak{F}}{\longleftrightarrow} \tilde{\Phi}^{m-n}(r,k). \tag{2.10}$$

Finally, using Euler's formula, the modulation property and the fact that the Fourier transform is linear, we have

$$\Phi(r,\phi,z)\cos(\phi) \overset{\mathfrak{F}}{\longleftrightarrow} \frac{1}{2}\left[\tilde{\Phi}^{m-1}(r,k) + \tilde{\Phi}^{m+1}(r,k)\right], \tag{2.11}$$

$$\Phi(r,\phi,z)\sin(\phi) \overset{\mathfrak{F}}{\longleftrightarrow} \frac{1}{2j}\left[\tilde{\Phi}^{m-1}(r,k) - \tilde{\Phi}^{m+1}(r,k)\right]. \tag{2.12}$$

This Fourier transform can now be used to solve the differential equation. Applying the forward transform to Equation 2.5 and using properties 2.8 and 2.9 results in

$$\frac{\partial^2\tilde{\Phi}}{\partial r^2}+\frac{1}{r}\frac{\partial\tilde{\Phi}}{\partial r}-\tilde{\Phi}(\frac{1}{r^2}m^2+k^2)=0. \tag{2.13}$$

Multiplying the above equation by r^2 and using the substitution $\tilde{\Phi}^m(r,k)=\tilde{F}_m(|k|r)=\tilde{F}_m(u)$, with $u=|k|r>0$, results in the differential equation for modified Bessel functions [18]

$$u^2\frac{\mathrm{d}^2\tilde{F}_m}{\mathrm{d}u^2}+u\frac{\mathrm{d}\tilde{F}_m}{\mathrm{d}u}-(m^2+u^2)\tilde{F}_m=0, \tag{2.14}$$

which has the general solution

$$\boxed{\tilde{F}_m(u)=\alpha_m(k)I_m(u)+\beta_m(k)K_m(u),} \tag{2.15}$$

where I_m is the modified Bessel function of the first kind and order m, K_m is the modified Bessel function of the second kind and order m, and $\alpha_m(k)$ and $\beta_m(k)$ are coefficients not dependent on r. The following properties are of importance:

$$|I_m(u)|\to\infty \quad \text{as} \quad u\to\infty \tag{2.16}$$

and

$$|K_m(u)|\to\infty \quad \text{as} \quad u\to 0. \tag{2.17}$$

Since all physical quantities are bounded, we observe from the above limiting forms that we have to set $\beta_m(k)$ to zero for the general solution in region I, while $\alpha_m(k)$ must be set to zero for the general solution in region II. Consequently, we have

$$\tilde{\Phi}^I=\alpha_m(k)I_m(|k|r), \tag{2.18}$$

and

$$\tilde{\Phi}^{II}=\beta_m(k)K_m(|k|r). \tag{2.19}$$

The components of the magnetic flux density can be found using Equation 2.3 as

$$B(r,\phi,z)=-\nabla\Phi=-\frac{\partial\Phi}{\partial r}\hat{\boldsymbol{r}}-\frac{1}{r}\frac{\partial\Phi}{\partial\phi}\hat{\boldsymbol{\phi}}-\frac{\partial\Phi}{\partial z}\hat{\boldsymbol{z}}. \tag{2.20}$$

Applying the Fourier transform and the corresponding differentiation properties results in

$$\tilde{B}^m(r,k)=-\frac{\partial\tilde{\Phi}}{\partial r}\hat{\boldsymbol{r}}-\frac{1}{r}jm\tilde{\Phi}\hat{\boldsymbol{\phi}}-jk\tilde{\Phi}\hat{\boldsymbol{z}}. \tag{2.21}$$

Equation 2.18 can be substituted into Equation 2.21 in order to find the components of the magnetic flux density in region I

$$\tilde{B}_r^I=-|k|\alpha_m(k)I_m'(|k|r), \tag{2.22}$$

$$\tilde{B}_\phi^I=-j\frac{m}{r}\alpha_m(k)I_m(|k|r), \tag{2.23}$$

$$\tilde{B}_z^I=-jk\alpha_m(k)I_m(|k|r). \tag{2.24}$$

The prime in Equation 2.22 indicates the derivative of the modified Bessel function with respect to its argument. Similarly, for region II we substitute Equation 2.19 in Equation 2.21 from which it follows that

$$\tilde{B}_r^{II}=-\beta_m(k)K_m'(|k|r)|k|\mathrm{d}k, \tag{2.25}$$

$$\tilde{B}_\phi^{II}=-jm\beta_m(k)K_m(|k|r), \tag{2.26}$$

$$\tilde{B}_z^{II}=-jk\beta_m(k)K_m(|k|r). \tag{2.27}$$

The next step involves using the electromagnetic boundary conditions to find a relationship between the expansion coefficients $\alpha_m(k),\beta_m(k)$ and $\boldsymbol{J_s}$. These boundary conditions are given by

$$\lim_{r\uparrow a}\hat{\boldsymbol{n}}\cdot\tilde{\boldsymbol{B}}^I=\lim_{r\downarrow a}\hat{\boldsymbol{n}}\cdot\tilde{\boldsymbol{B}}^{II}, \tag{2.28}$$

$$\lim_{r\downarrow a} \hat{\boldsymbol{n}} \times \tilde{\boldsymbol{B}}^{II} - \lim_{r\uparrow a} \hat{\boldsymbol{n}} \times \tilde{\boldsymbol{B}}^{I} = \mu_0 \tilde{\boldsymbol{J}}_s. \tag{2.29}$$

The first boundary condition states that the normal components of magnetic flux density must be continuous across the surface of the cylinder with radius $r = a$. The second boundary condition states that the difference between the tangential components of $\tilde{\boldsymbol{B}}$ is determined by the surface current density.

Since the r component of the magnetic flux density is normal to the cylindrical surface, Equation 2.28 becomes

$$\lim_{r\uparrow a} \tilde{B}_r^I = \lim_{r\downarrow a} \tilde{B}_r^{II} \tag{2.30}$$

and substituting the corresponding fields from Equation 2.22 and 2.25 into the above leads to the following relation between the expansion coefficients

$$\alpha_m(k) I_m(|k|a) = \beta_m(k) K_m(|k|a), \tag{2.31}$$

which can be summarized as

$$\boxed{\beta_m(k) = \alpha_m(k) \frac{I'_m(|k|a)}{K'_m(|k|a)}.} \tag{2.32}$$

The second boundary condition (Equation 2.29) is used to find a relationship between the expansion coefficient and the current density. The magnetic flux density has two tangential components with respect to the cylinder surface, namely, $\tilde{B}_\phi$ and $\tilde{B}_z$. For the z-component we have

$$\lim_{r\downarrow a} \tilde{B}_\phi^{II} - \lim_{r\uparrow a} \tilde{B}_\phi^{I} = \mu_0 \tilde{J}_{s:z}^m, \tag{2.33}$$

while for the ϕ-component we obtain

$$-\lim_{r\downarrow a} \tilde{B}_z^{II} + \lim_{r\uparrow a} \tilde{B}_z^{I} = \mu_0 \tilde{J}_{s:\phi}^m. \tag{2.34}$$

Starting with Equation 2.33 and substitution Equation 2.23 and 2.26 results in

$$jm\left[\alpha_m(k) I_m(|k|a) - \beta_m(k) K_m(|k|a)\right] = \mu_0 a \tilde{J}_{s:z}^m. \tag{2.35}$$

from which we observe that

$$\boxed{\tilde{J}_{s:z}^{m=0}(r,k) = 0 \quad k \in \mathbb{R}.} \tag{2.36}$$

Finally, substitute Equations 2.24 and 2.27 in Equation 2.34 to obtain

$$-jk\left[\alpha_m(k) I_m(|k|a) - \beta_m(k) K_m(|k|a)\right] = \mu_0 \tilde{J}_{s:\phi}^m(r,k) \tag{2.37}$$

from which it follows that we must have

$$\boxed{\tilde{J}_{s:\phi}^m(r, k=0) = 0 \quad m \in \mathbb{Z}.} \tag{2.38}$$

Using Equations 2.35 and 2.37 we can find a relationship between $\tilde{J}_{s:z}^m$ and $\tilde{J}_{s:\phi}^m$. Explicitly, we have

$$\boxed{ka\tilde{J}_{s:z}^m + m\tilde{J}_{s:\phi}^m = 0} \tag{2.39}$$

This is the continuity equation in the spatial Fourier domain. Now using the inverse Fourier transform we can obtain

$$\frac{\partial J_{s:z}}{\partial z} + \frac{1}{a}\frac{\partial J_{s:\phi}}{\partial \phi} = 0. \tag{2.40}$$

This is the continuity equation for the current density. Which can be written as

$$\nabla \cdot \boldsymbol{J_s} = \boldsymbol{0} \tag{2.41}$$

The relationship between the expansion coefficient α and the current density can now be found. Substituting Equation 2.32 in Equation 2.37 gives

$$jk\alpha_m(k) \frac{I_m(|k|a)K'_m(|k|a) - I'_m(|k|a)K_m(|k|a)}{K'_m(|k|a)} = \mu_0 \tilde{J}_{s:\phi}^m \tag{2.42}$$

and using the Wronskian of the modified Bessel function [18], the numerator of the above equation can be written as

$$I_m(|k|a)K'_m(|k|a) - I'_m(|k|a)K_m(|k|a) = -\frac{1}{|k|a}. \tag{2.43}$$

Substituting the above into Equation 2.42 and rewriting for $\alpha_m(k)$, we arrive at

$$\boxed{\alpha_m(k) = -ja\mu_0 \frac{|k|}{k} K'_m(|k|a)\tilde{J}^m_{s:\phi}.} \tag{2.44}$$

The expansion coefficient $\beta_m(k)$ can be found using the above equation and Equation 2.32, explicitly we have

$$\boxed{\beta_m(k) = -ja\mu_0 \frac{|k|}{k} I'_m(|k|a)\tilde{J}^m_{s:\phi}.} \tag{2.45}$$

These expansion coefficients can easily be found in terms of the z-component of the current density using the continuity equation. As the focus of this work lies on the design of gradient coils, region I is only of interest. Region II can be used for shielding purposes [10]. The components of the magnetic flux density in region I are now found as follows. The coefficient $\alpha_m(k)$ (Equation 2.45) is substituted in Equations 2.22, 2.23, and 2.24. The inverse Fourier transform is then applied resulting in

$$\boxed{B^I_r = \frac{ja\mu_0}{4\pi^2} \int_{k=-\infty}^{\infty} \sum_{m=-\infty}^{\infty} k\tilde{J}^m_{s:\phi} I'_m(|k|r)K'_m(|k|a)e^{jkz}e^{jm\phi}\mathrm{d}k,} \tag{2.46}$$

$$\boxed{B^I_\phi = -\frac{a\mu_0}{4\pi^2 r} \int_{k=-\infty}^{\infty} \sum_{m=-\infty}^{\infty} m\frac{|k|}{k}\tilde{J}^m_{s:\phi} I_m(|k|r)K'_m(|k|a)e^{jkz}e^{jm\phi}\mathrm{d}k,} \tag{2.47}$$

$$\boxed{B^I_z = -\frac{a\mu_0}{4\pi^2} \int_{k=-\infty}^{\infty} \sum_{m=-\infty}^{\infty} |k|\tilde{J}^m_{s:\phi} I_m(|k|r)K'_m(|k|a)e^{jkz}e^{jm\phi}\mathrm{d}k.} \tag{2.48}$$

The magnetic flux density oriented in the x-direction is found using the following equation

$$B^I_x = B^I_r \cos\phi - B^I_\phi \sin\phi. \tag{2.49}$$

Before moving on and finding an expression for the current density the following section will discuss the target fields which will be prescribed.

2.2. TARGET GRADIENT FIELDS

The fields chosen in this section simplify the target field approach. The total desired magnetic flux density inside the bore of the magnet can be written as a sum of the main magnetic field and the gradient field terms

$$\boldsymbol{B}(x,y,z) = B_0\hat{\boldsymbol{x}} + (xg_x + yg_y + zg_z)\hat{\boldsymbol{x}}. \tag{2.50}$$

Here, B_0 is the main magnetic field and is assumed to be homogeneous inside the volume of interest. The g_x, g_y, g_z terms are the gradient field strengths in $\mathrm{Vs/m^3}$ or $\mathrm{T/m}$ corresponding to the three gradient coils. These field strengths are multiplied by the coordinates x, y and z to generate linearity.

The target fields will be defined on the surface of a cylinder with infinite length and radius $b < a$ and not in a volume as one would expect. This is done in order to allow inversion of the target field equations. Choosing a different target cylinder radius will not change the wire pattern. The gradient fields are written in cylindrical coordinates in Equation 2.51. Vector plots showing the behavior of these target fields are shown in Figure 2.2. The figure shows the desired behavior for each target field on a cylinder surface. It should be observed that the target fields of the x- and y-gradient are independent of z, the z-gradient is independent of ϕ. Using cylindrical coordinates the target fields can be written as

$$\boldsymbol{G}_{x,y,z}(b,\phi,z) = \begin{cases} b\cos(\phi)g_x\hat{\boldsymbol{x}} & \text{x-gradient} \\ b\sin(\phi)g_y\hat{\boldsymbol{x}} & \text{y-gradient} \\ zg_z\hat{\boldsymbol{x}} & \text{z-gradient} \end{cases} \tag{2.51}$$

In order for the gradient coils to be physically feasible and not of infinite length, the fields should only behave

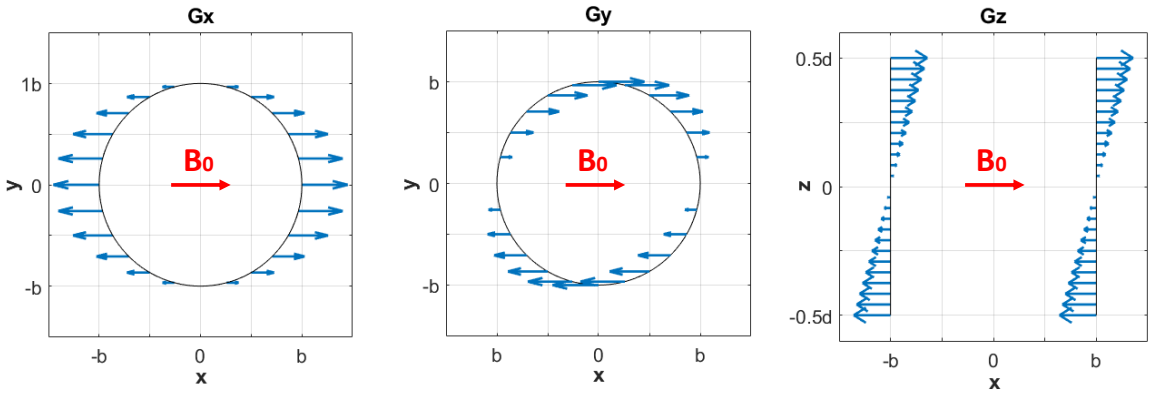

Figure 2.2: Vector plots of the desired gradient fields. From left to right: the x- and y-gradient on a cylinder with radius b are constant with respect to z. The z-gradient as seen from a top view, constant with respect to ϕ.

as shown in Figure 2.2 inside a certain desired region. The length of this region in the z-direction is denoted with the parameter d. The field should go to zero outside this region. To obtain this behavior the following function is introduced

$$\Gamma(z) = \frac{1}{1+(z/d)^n}. \tag{2.52}$$

This is a smooth block-like function and the target fields from Equation 2.51 will be multiplied by it. The function is equal to one inside the desired region making the x- and y-gradient independent of z, as is required. The parameter n should be an even integer. Choosing a higher value for n will stretch the region d and make the function sharper. For the z-gradient the following function arises due to the multiplication by z:

$$\Gamma_z(z) = \frac{z}{1+(z/d)^n}. \tag{2.53}$$

This function behaves linearly within the region with length d. Higher n again result in a faster decay and a longer desired region. Important to note is that in order to satisfy Equation 2.38 the z-dependent part of the target field must satisfy the following equation

$$\tilde{G}(0) = \int_{z=-\infty}^{\infty} G(z)\mathrm{d}z = 0. \tag{2.54}$$

The above holds for the function Γ_z. This is not the case with Γ. In order for the Fourier transform to converge it needs to be altered slightly. By adding Γ as negative side-lobes with half the desired length on both sides we obtain an equation that satisfies the above relation. This can be written as

$$\Gamma_{xy}(z,d) = \Gamma(z,d) - [\Gamma(z-\alpha, 0.5d) + \Gamma(z+\alpha, 0.5d)]. \tag{2.55}$$

When choosing $\alpha \geq 3d$ this satisfies Equation 2.54. The functions Γ_{xy} and Γ_z are plotted in Figure 2.3 for different n.

The functions allow easy alteration of the desired region length through the parameter d. In addition, n gives freedom in the design with respect to the accuracy of the desired region and how fast the field is required to go to zero. For short coils, n can be chosen large in order for the field taper off faster. Choosing larger n also has drawbacks, high current densities are needed to force the field to zero outside the desired region. This can result in a design which is not physically feasible due to the coil turns being too close together. The target fields can now be written as

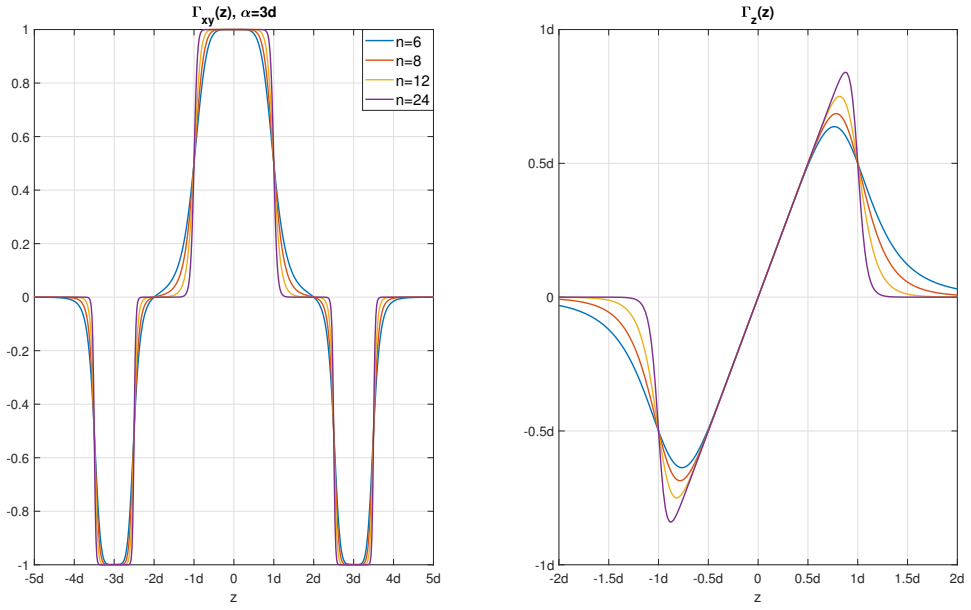

Figure 2.3: The functions used to shape the target fields in the z-direction for different values of the sharpness parameter n. On the left the function used for the x- and y-gradient, on the right-hand side the function used for the z-gradient.

$$\boldsymbol{G}_{x,y,z}(b,\phi,z) = \begin{cases} \Gamma_{xy}(z)\, b\cos(\phi)\, g_x \hat{\boldsymbol{x}} & \text{x-gradient} \\ \Gamma_{xy}(z)\, b\sin(\phi)\, g_y \hat{\boldsymbol{x}} & \text{y-gradient} \\ \Gamma_z(z)\, g_z \hat{\boldsymbol{x}} & \text{z-gradient} \end{cases} \tag{2.56}$$

At a later stage, the Fourier transform of these target fields will be required. Using the modulation property of the Fourier transform, these transforms are given by

$$\tilde{\boldsymbol{G}}_x^m(k) = \begin{cases} \tilde{\Gamma}_{xy}(k)\, g_x \pi b \hat{\boldsymbol{x}} & m = 1, -1 \\ 0 & \text{otherwise,} \end{cases} \tag{2.57}$$

$$\tilde{\boldsymbol{G}}_y^m(k) = \begin{cases} -j\tilde{\Gamma}_{xy}(k)\, g_y \pi b \hat{\boldsymbol{x}} & m = 1 \\ j\tilde{\Gamma}_{xy}(k)\, g_y \pi b \hat{\boldsymbol{x}} & m = -1 \\ 0 & \text{otherwise,} \end{cases} \tag{2.58}$$

$$\tilde{\boldsymbol{G}}_z^m(k) = \begin{cases} \tilde{\Gamma}_z(k)\, g_z 2\pi \hat{\boldsymbol{x}} & m = 0 \\ 0 & \text{otherwise,} \end{cases} \tag{2.59}$$

where $\tilde{\Gamma}_{xy}(k)$ and $\tilde{\Gamma}_z(k)$ are the one-dimensional Fourier transforms of $\Gamma_{xy}(z)$ and $\Gamma_z(z)$, respectively. Having these transforms available, we are now in a position to apply the target field method.

2.3. GRADIENT COILS FOR LOW FIELD MRI

What remains is substituting the target fields and rewriting the equations in terms of the current density. The relationship between the current density and the target field can be written in terms of the cylindrical components found earlier

$$B_x = B_r \cos\phi - B_\phi \sin\phi. \tag{2.60}$$

All the work from here on is done in region I. Substituting Equations 2.46 and 2.47 into the above and taking the target field on a cylinder with constant radius b results in

$$\begin{aligned} B_x(b,\phi,z) = {} & \frac{ja\mu_0}{4\pi^2} \int_{k=-\infty}^{\infty} \sum_{m=-\infty}^{\infty} k\tilde{J}_{s:\phi}^m I'_m(|k|b) K'_m(|k|a) \cos(\phi) e^{jkz} e^{jm\phi} \mathrm{d}k \\ & + \frac{a\mu_0}{4\pi^2 b} \int_{k=-\infty}^{\infty} \sum_{m=-\infty}^{\infty} m\frac{|k|}{k} \tilde{J}_{s:\phi}^m I_m(|k|b) K'_m(|k|a) \sin(\phi) e^{jkz} e^{jm\phi} \mathrm{d}k. \end{aligned} \tag{2.61}$$

This is the forward operator with which the magnetic flux densities in the x-direction can be found corresponding to a prescribed current. This equation will now be inverted. Before doing so, however, we first introduce the quantities

$$\tilde{P}^m(k) = a\mu_0 k I'_m(|k|b)K'_m(|k|a), \tag{2.62}$$

$$\tilde{Q}^m(k) = m\frac{a\mu_0}{b}\frac{|k|}{k}I_m(|k|b)K'_m(|k|a). \tag{2.63}$$

Since the modified Bessel functions are identical for opposite but equal order [18] the following properties can be distinguished

$$\tilde{P}^m(k) = \tilde{P}^{-m}(k), \tag{2.64}$$

$$\tilde{Q}^m(k) = -\tilde{Q}^{-m}(k). \tag{2.65}$$

In addition, $\tilde{Q}^0 = 0$. Substituting $\tilde{P}$ and $\tilde{Q}$ into expression 2.61 yields the following

$$\begin{aligned} B_x(b,\phi,z) = &\frac{j}{4\pi^2}\int_{k=-\infty}^{\infty}\sum_{m=-\infty}^{\infty}\tilde{J}^m_{s:\phi}\tilde{P}^m\cos(\phi)e^{jkz}e^{jm\phi}\mathrm{d}k \\ &+\frac{1}{4\pi^2}\int_{k=-\infty}^{\infty}\sum_{m=-\infty}^{\infty}\tilde{J}^m_{s:\phi}\tilde{Q}^m\sin(\phi)e^{jkz}e^{jm\phi}\mathrm{d}k. \end{aligned} \tag{2.66}$$

Applying the Fourier transform to the above equation and using the modulation property results in

$$\tilde{B}^m_x(k) = \frac{j}{2}\left[\tilde{J}^{m+1}_{s:\phi}\tilde{P}^{m+1} + \tilde{J}^{m-1}_{s:\phi}\tilde{P}^{m-1}\right] + \frac{1}{2j}\left[\tilde{J}^{m-1}_{s:\phi}\tilde{Q}^{m-1} - \tilde{J}^{m+1}_{s:\phi}\tilde{Q}^{m+1}\right], \tag{2.67}$$

which can be also be written as

$$\tilde{B}^m_x(k) = \frac{j}{2}\left[\tilde{J}^{m+1}_{s:\phi}\left(\tilde{P}^{m+1} + \tilde{Q}^{m+1}\right) + \tilde{J}^{m-1}_{s:\phi}\left(\tilde{P}^{m-1} - \tilde{Q}^{m-1}\right)\right]. \tag{2.68}$$

The right-hand side is now dictated by the modes of the magnetic flux density. Due to modulation even numbered modes of the magnetic flux density result in odd modes of the current density. In the following sub-sections the target gradient fields $\tilde{G}^m_{x,y,z}$ stated in Section 2.2 are substituted. This makes the equation specific to the corresponding gradient coil.

CURRENT DENSITY Z-GRADIENT

The z-gradient has a non-zero solution for the mode $m = 0$. This main mode causes the odd numbered modes $m = \pm 1$ on the right-hand side. For all other modes $\tilde{G}_z = 0$. The modulation then determines that only the odd numbered modes on the right-hand side can influence the main mode. This can be shown by taking m odd: $m = 2n+1$, resulting in even current density modes

$$\tilde{G}^{2n+1}_z = \frac{j}{2}\left[\tilde{J}^{2n+2}_{s:\phi}\left(\tilde{P}^{2n+2} + \tilde{Q}^{2n+2}\right) + \tilde{J}^{2n}_{s:\phi}\left(\tilde{P}^{2n} - \tilde{Q}^{2n}\right)\right]. \tag{2.69}$$

In the above equation $\tilde{G}^{2n+1}_z$ is zero for all n. The equation is only satisfied if all even modes of the current density are set to zero. This leaves the odd numbered modes of the current density. The substitution $m = 2n$ is made in order to only consider the odd modes on the right-hand side. Equation 2.68 is written as

$$\tilde{G}^{2n}_z(k) = \frac{j}{2}\left[\tilde{J}^{2n+1}_{s:\phi}\left(\tilde{P}^{2n+1} + \tilde{Q}^{2n+1}\right) + \tilde{J}^{2n-1}_{s:\phi}\left(\tilde{P}^{2n-1} - \tilde{Q}^{2n-1}\right)\right]. \tag{2.70}$$

Starting with $n = 0$, for which $\tilde{G}^{2n}_z(k)$ has a non-zero solution

$$\tilde{G}^0_z(k) = \frac{j}{2}\left[\tilde{J}^1_{s:\phi}\left(\tilde{P}^1 + \tilde{Q}^1\right) + \tilde{J}^{-1}_{s:\phi}\left(\tilde{P}^{-1} - \tilde{Q}^{-1}\right)\right]. \tag{2.71}$$

The assumption is made that $\tilde{J}^m_{s:\phi}$ is an even function of m.

$$\tilde{J}^m_{s:\phi} = \tilde{J}^{-m}_{s:\phi}. \tag{2.72}$$

From this it follows that $J_{s:\phi}$ is automatically an even function of ϕ. Using the above property and the ones stated in 2.64 and 2.65, the following can be written

$$\tilde{J}^1_{s:\phi} = -\frac{j\tilde{G}^0_z}{\tilde{P}^1 + \tilde{Q}^1}. \tag{2.73}$$

The same can be done for the mode $n = 1$. Starting again from Equation 2.74 and substituting the corresponding modes

$$0 = \frac{j}{2}\left[\tilde{J}^3_{s:\phi}\left(\tilde{P}^3 + \tilde{Q}^3\right) + \tilde{J}^1_{s:\phi}\left(\tilde{P}^1 - \tilde{Q}^1\right)\right]. \tag{2.74}$$

This higher order mode has a relationship with the main mode. The above can be rewritten as

$$\tilde{J}^3_{s:\phi} = -\frac{\tilde{P}^1 - \tilde{Q}^1}{\tilde{P}^3 + \tilde{Q}^3}\tilde{J}^1_{s:\phi}. \tag{2.75}$$

Taking $n = -1$ results in the same equation as written above. This confirms the even assumption made in equation 2.72. Substituting Equation 2.73 into the above results in

$$\tilde{J}^3_{s:\phi} = \frac{\tilde{P}^1 - \tilde{Q}^1}{\tilde{P}^3 + \tilde{Q}^3}\frac{j\tilde{G}^0_z}{\tilde{P}^1 + \tilde{Q}^1}. \tag{2.76}$$

The following is found for $n = 2$

$$\tilde{J}^5_{s:\phi} = -\frac{\tilde{P}^3 - \tilde{Q}^3}{\tilde{P}^5 + \tilde{Q}^5}\frac{\tilde{P}^1 - \tilde{Q}^1}{\tilde{P}^3 + \tilde{Q}^3}\frac{j\tilde{G}^0_z}{\tilde{P}^1 + \tilde{Q}^1}. \tag{2.77}$$

It can be concluded that all uneven modes of the current density are excited. The current density can thus be obtained by taking the summation of the inverse Fourier transforms with respect to these odd modes. The equal modes but opposite sign result in a cosine term. An apodization function $T(k)$ is introduced

$$T(k) = e^{-2(kh)^2}. \tag{2.78}$$

This Gaussian can be seen as the regularization function which assists the Fourier transform to converge. Numerical experiments show that $h = 0.1$ gives reasonable convergence. The ϕ component of the current density can be written as

$$\boxed{J^z_{s:\phi} = j\frac{1}{2\pi^2}\sum_{n=0}^{\infty}(-1)^{n+1}\cos\left[(2n+1)\phi\right]\int_{k=-\infty}^{\infty}\frac{\tilde{G}^0_z(k)\,T(k)}{\tilde{P}^1 + \tilde{Q}^1}\prod_{m=0}^{n}\frac{\tilde{P}^{2m-1} - \tilde{Q}^{2m-1}}{\tilde{P}^{2m+1} + \tilde{Q}^{2m+1}}e^{jkz}\mathrm{d}k.} \tag{2.79}$$

The superscript indicates that this is the current density corresponding to the z-gradient. Using continuity Equation (2.40) for the current density we can find the z-component of the current density as

$$\boxed{J^z_{s:z} = \frac{1}{2\pi^2 a}\sum_{n=0}^{\infty}(-1)^{n+1}(2n+1)\sin\left[(2n+1)\phi\right]\int_{k=-\infty}^{\infty}\frac{1}{k}\frac{\tilde{G}^0_z(k)\,T(k)}{\tilde{P}^1 + \tilde{Q}^1}\prod_{m=0}^{n}\frac{\tilde{P}^{2m-1} - \tilde{Q}^{2m-1}}{\tilde{P}^{2m+1} + \tilde{Q}^{2m+1}}e^{jkz}\mathrm{d}k.} \tag{2.80}$$

It will become clear that the modes which have a non-zero solution for the gradient fields will play a dominate role, these will be called the main modes. Taking only this main mode ($n = 0$), substituting $\tilde{P}$ and $\tilde{Q}$ and the target field results in the following

$$\tilde{J}^{\pm1}_{s:\phi}(k) = -j\frac{g_z}{a\mu_0}\frac{2\pi\tilde{\Gamma}_z(k)\,T(k)}{\frac{|k|}{k}K_1'(|k|a)\left[|k|I_1'(|k|b) + \frac{1}{b}I_1(|k|b)\right]} \tag{2.81}$$

Taking the inverse Fourier transform of this mode

$$J^{\pm1}_{s:\phi}(a,\phi,z) = -j\frac{g_z}{a\mu_0}\frac{1}{4\pi^2}\sum_{m=\pm1}\int_{k=-\infty}^{\infty}\frac{2\pi\tilde{\Gamma}_z(k)\,T(k)}{\frac{|k|}{k}K_1'(|k|a)\left[|k|I_1'(|k|b) + \frac{1}{b}I_1(|k|b)\right]}e^{j\phi m}e^{jkz}\mathrm{d}k. \tag{2.82}$$

This can be written as

$$J^{\pm1}_{s:\phi}(a,\phi,z) = -j\frac{g_z}{\pi a\mu_0}\cos(\phi)\int_{k=-\infty}^{\infty}\frac{\tilde{\Gamma}_z(k)\,T(k)}{\frac{|k|}{k}K_1'(|k|a)\left[|k|I_1'(|k|b) + \frac{1}{b}I_1(|k|b)\right]}e^{jkz}\mathrm{d}k \tag{2.83}$$

The current densities and stream functions for all three gradient coils corresponding to the main mode are summarized in Table 2.1.

CURRENT DENSITIES X- AND Y-GRADIENT

The x- and y-gradient target field have a non-zero solution for the modes $m = \pm 1$. This leads to even modes on the right-hand side. Only the even modes of the current density play a part for the x- and y-gradient. The substitution $m = 2n+1$ is made in order to ensure this, leading to the following

$$\tilde{G}^{2n+1}_{x,y}(k) = \frac{j}{2}\left[\tilde{J}^{2n+2}_{s:\phi}\left(\tilde{P}^{2n+2} + \tilde{Q}^{2n+2}\right) + \tilde{J}^{2n}_{s:\phi}\left(\tilde{P}^{2n} - \tilde{Q}^{2n}\right)\right]. \tag{2.84}$$

The modes $n = 0$ and $n = -1$ yield non-zero solutions for the magnetic flux density. Starting with $n = 0$

$$\tilde{G}^{1}_{x,y}(k) = \frac{j}{2}\left[\tilde{J}^{2}_{s:\phi}\left(\tilde{P}^{2} + \tilde{Q}^{2}\right) + \tilde{J}^{0}_{s:\phi}\left(\tilde{P}^{0} - \tilde{Q}^{0}\right)\right]. \tag{2.85}$$

$\tilde{J}_{s:\phi}$ is now said to be an even function of m. Furthermore, $\tilde{J}^0_{s:\phi}$ is set to zero because this current density results in current loops in the ϕ-direction ($\tilde{J}^0_{s:z} = 0$). These currents are responsible for the z-components of the magnetic field. This is a concomitant component which we are not interested in. Applying these two properties we arrive at

$$\tilde{G}^{1}_{x,y}(k) = \frac{j}{2}\tilde{J}^{2}_{s:\phi}\left(\tilde{P}^{2} + \tilde{Q}^{2}\right), \tag{2.86}$$

which can be written as

$$\tilde{J}^{2}_{s:\phi} = -2j\frac{\tilde{G}^{1}_{x}(k)}{\tilde{P}^{2} + \tilde{Q}^{2}}. \tag{2.87}$$

Taking the mode $n = -1$ leads to the same result as above for the x-gradient because $\tilde{G}^1_x = \tilde{G}^{-1}_x$. For the y-gradient however $\tilde{G}^1_y = -\tilde{G}^{-1}_y$. This will be important when adding the modes. Moving on to the higher order modes, substituting $n = 1$ gives

$$0 = \frac{j}{2}\left[\tilde{J}^{4}_{s:\phi}\left(\tilde{P}^{4} + \tilde{Q}^{4}\right) + \tilde{J}^{2}_{s:\phi}\left(\tilde{P}^{2} - \tilde{Q}^{2}\right)\right]. \tag{2.88}$$

Again a relationship with the main mode is found. Rewriting the above for $\tilde{J}^4_{s:\phi}$

$$\tilde{J}^{4}_{s:\phi} = -\frac{\tilde{P}^{2} - \tilde{Q}^{2}}{\tilde{P}^{4} + \tilde{Q}^{4}}\tilde{J}^{2}_{s:\phi}, \tag{2.89}$$

and substituting $\tilde{J}^2_{s:\phi}$, we obtain

$$\tilde{J}^{4}_{s:\phi} = 2j\frac{\tilde{P}^{2} - \tilde{Q}^{2}}{\tilde{P}^{4} + \tilde{Q}^{4}}\frac{\tilde{G}^{1}_{x}(k)}{\tilde{P}^{2} + \tilde{Q}^{2}}. \tag{2.90}$$

The general solution for the current density can be created by taking all even modes of the current density into account. The equal modes but with opposite sign result in a cosine term for the x-gradient

$$\boxed{J^{x}_{s:\phi} = j\frac{1}{\pi^2}\sum_{n=0}^{\infty}(-1)^{n+1}\cos\left[(2n+2)\phi\right]\int_{k=-\infty}^{\infty}\frac{\tilde{G}^{1}_{x}(k)\,T(k)}{\tilde{P}^{2} + \tilde{Q}^{2}}\prod_{m=0}^{n}\frac{\tilde{P}^{2n} - \tilde{Q}^{2n}}{\tilde{P}^{2n+2} + \tilde{Q}^{2n+2}}e^{jkz}\mathrm{d}k.} \tag{2.91}$$

Using the continuity equation, the z-component is found to be

$$\boxed{J^{x}_{s:z} = \frac{1}{\pi^2 a}\sum_{n=0}^{\infty}(-1)^{n+1}(2n+2)\sin\left[(2n+2)\phi\right]\int_{k=-\infty}^{\infty}\frac{1}{k}\frac{\tilde{G}^{1}_{x}(k)\,T(k)}{\tilde{P}^{2} + \tilde{Q}^{2}}\prod_{m=0}^{n}\frac{\tilde{P}^{2n} - \tilde{Q}^{2n}}{\tilde{P}^{2n+2} + \tilde{Q}^{2n+2}}e^{jkz}\mathrm{d}k.} \tag{2.92}$$

The y-gradient is similar to the x-gradient only the summation of the equal modes but opposite sign result in a sine term

$$\boxed{J^{y}_{s:\phi} = -\frac{1}{\pi^2}\sum_{n=0}^{\infty}(-1)^{n+1}\sin\left[(2n+2)\phi\right]\int_{k=-\infty}^{\infty}\frac{\tilde{G}^{1}_{y}(k)\,T(k)}{\tilde{P}^{2} + \tilde{Q}^{2}}\prod_{m=0}^{n}\frac{\tilde{P}^{2n} - \tilde{Q}^{2n}}{\tilde{P}^{2n+2} + \tilde{Q}^{2n+2}}e^{jkz}\mathrm{d}k.} \tag{2.93}$$

The z-component is found to be

$$\boxed{J^{y}_{s:z} = -j\frac{1}{\pi^2 a}\sum_{n=0}^{\infty}(-1)^{n+1}(2n+2)\cos\left[(2n+2)\phi\right]\int_{k=-\infty}^{\infty}\frac{1}{k}\frac{\tilde{G}^{1}_{y}(k)\,T(k)}{\tilde{P}^{2} + \tilde{Q}^{2}}\prod_{m=0}^{n}\frac{\tilde{P}^{2n} - \tilde{Q}^{2n}}{\tilde{P}^{2n+2} + \tilde{Q}^{2n+2}}e^{jkz}\mathrm{d}k.} \tag{2.94}$$

2.4. STREAM FUNCTIONS

The current density derived in the previous section will now be approximated using discrete current paths in order to create a gradient coil. This is done using stream functions. These functions are commonly used in aero- and hydrodynamics to obtain information on the flow of particles [19]. In this case the flow of particles will be the flow of charged particles. The objective is to obtain a function that combines the two current density components $J_{s:\phi}$ and $J_{s:z}$. The functions will assist with the current path placement. In this section the stream functions for the current density on the cylinder surface will be derived. Furthermore, some useful features of the stream function will be shown. At the end the stream functions for the three gradient coils are given.

Equation 2.41 shows us that the current density can be written as the curl of a vector potential. This vector potential is defined as the stream function $\boldsymbol{\psi}(\phi, z) = \psi(\phi, z)\hat{\boldsymbol{r}}$ with units ampere. This can be written as

$$\boldsymbol{J_s} = \nabla \times \psi(\phi, z)\hat{\boldsymbol{r}}. \tag{2.95}$$

Computing the curl of the stream function results in

$$\boldsymbol{J_s} = \frac{\partial \psi}{\partial z}\hat{\boldsymbol{\phi}} - \frac{1}{a}\frac{\partial \psi}{\partial \phi}\hat{\boldsymbol{z}}. \tag{2.96}$$

This can be written out in components as

$$J_{s:\phi} = \frac{\partial \psi}{\partial z}, \tag{2.97}$$

$$J_{s:z} = -\frac{1}{a}\frac{\partial \psi}{\partial \phi}. \tag{2.98}$$

Substituting Equations 2.97 and 2.98 into Equation 2.40 shows that the stream function indeed satisfies the continuity equation. The stream function can thus be obtained through integration. The integration constant that arises can be determined using the continuity equation.

The current density $\boldsymbol{J}_s$ is tangential to a streamline in every point. If we take a vector $d\boldsymbol{u}$ tangent to the current density vector the cross product has to equal zero

$$\mathrm{d}\boldsymbol{u} \times \boldsymbol{J_s} = \boldsymbol{0}. \tag{2.99}$$

In cylindrical coordinates $\mathrm{d}\boldsymbol{u}$ and $\boldsymbol{J_s}$ can be written in the following components

$$\mathrm{d}\boldsymbol{u} = \hat{\boldsymbol{r}}\mathrm{d}r + \hat{\boldsymbol{\phi}}r\mathrm{d}\phi + \hat{\boldsymbol{z}}\mathrm{d}z, \tag{2.100}$$

$$\boldsymbol{J_s} = \hat{\boldsymbol{r}}J_{s:r} + \hat{\boldsymbol{\phi}}J_{s:\phi} + \hat{\boldsymbol{z}}J_{s:z}. \tag{2.101}$$

The current density was defined on the cylindrical surface with the radius equal to a. The r component of the current density is equal to zero. Computing Equation 2.99 results in

$$J_{s:z}a\mathrm{d}\phi - J_{s:\phi}\mathrm{d}z = 0, \tag{2.102}$$

This can be rewritten as

$$\frac{\mathrm{d}z}{\mathrm{d}\phi} = \frac{J_{s:z}a}{J_{s:\phi}}. \tag{2.103}$$

This is the differential equation for a streamline on the cylinder surface. Now it will be shown how the stream function relates to this streamline. Taking the derivative of the stream function and using the chain rule

$$\mathrm{d}\psi = \frac{\partial \psi}{\partial \phi}\mathrm{d}\phi + \frac{\partial \psi}{\partial z}\mathrm{d}z. \tag{2.104}$$

Substituting equations 2.97 and 2.98 into the above expression results in

$$\mathrm{d}\psi = -aJ_{s:z} + J_{s:\phi}. \tag{2.105}$$

For curves on which ψ is constant its derivative equals zero. Substituting this, we obtain

$$0 = -aJ_{s:z}\mathrm{d}\phi + J_{s:\phi}\mathrm{d}z, \tag{2.106}$$

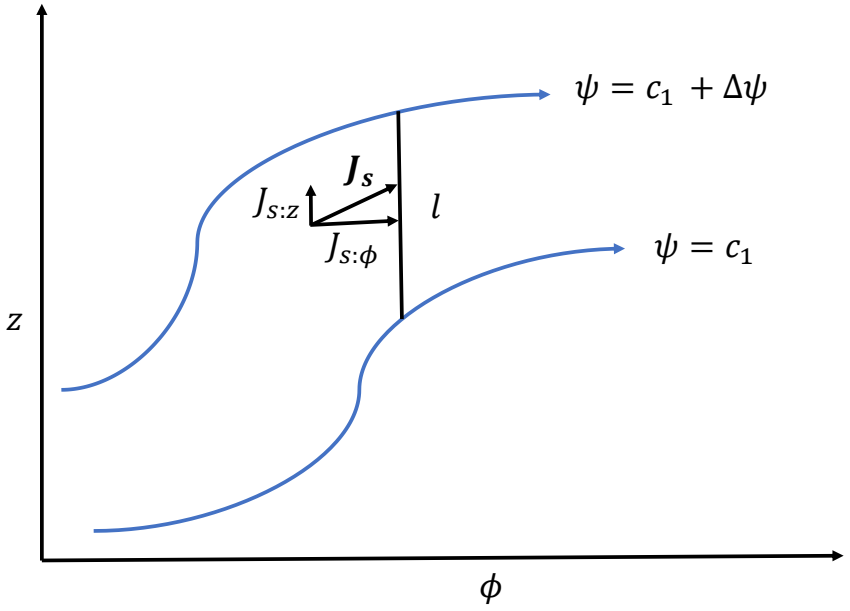

Figure 2.4: Two streamlines and the current density that flows between them.

which is equal to the differential equation for the streamline defined earlier

$$\frac{aJ_{s:z}}{J_{s:\phi}} = \frac{\mathrm{d}z}{\mathrm{d}\phi}. \tag{2.107}$$

It can thus be concluded that constant values of the stream function represent streamlines. And that the current density is tanget to these lines at every point. these lines are tangent to the current density vector in every point.

The following shows the relationship between the streamlines and current. Suppose there are two streamlines having constant values for the stream function c_1 and $c_1 + \Delta\psi$. Between the two streamlines there is a current density flow denoted by the vector $\boldsymbol{J_s}$. The flow between the two streamlines can be thought of as a stream tube through which the flow is constant. Figure 2.4 shows this topology. The current flowing in the tube can be calculated in the following manner. First a line in the z-direction is taken between the two streamlines. We have shown that the current density is conservative on the cylinder so there is no path dependency. The current is equal to the current density passing through the line this can be computed by integrating the components of $\boldsymbol{J_s}$ normal to the line which is written as

$$I = \int_l J_{s:\phi}\mathrm{d}z. \tag{2.108}$$

Substituting Equations 2.97 gives us

$$I = \int_l \frac{\partial\psi}{\partial z}\mathrm{d}z. \tag{2.109}$$

When inserting the boundaries this can be written as

$$I = \int_{c1}^{c1+\Delta\psi} \mathrm{d}\psi. \tag{2.110}$$

Computing the integral we find

$$I = \Delta\psi. \tag{2.111}$$

The current between two streamlines is thus equal to the difference in streamline level. The current density between two streamlines can be approached by placing a conductor between the two streamlines. The current value being equal to the difference in streamline amplitude. The gradient coil should preferably be built

using a single wire or path. This can be done by keeping the difference between stream function value of adjacent streamlines constant. Resulting in constant current and distributed paths. This is achieved by contour plotting the stream function and placing current paths between these lines. The current paths can then be connected in series to form a coil.

The value of the stream function dictates the current direction. This can be deducted from Equation 2.95. $\hat{\boldsymbol{r}}$ points out of the cylinder surface. With the right-hand rule it can be shown that a positive $\boldsymbol{\psi}$ corresponds to a counterclockwise current, negative $\boldsymbol{\psi}$ corresponds to clockwise current.

The winding patterns can be obtained by integration of Equations 2.91, 2.93 and 2.83. The integration constant is found to be zero. This results in the stream functions written below

$$\boxed{\psi^x(\phi,z) = \frac{1}{\pi^2}\sum_{n=0}^{\infty}(-1)^{n+1}\cos\left[(2n+2)\phi\right]\int_{k=-\infty}^{\infty}\frac{1}{k}\frac{\tilde{G}_x^1(k)T(k)}{\tilde{P}^2+\tilde{Q}^2}\prod_{m=0}^{n}\frac{\tilde{P}^{2n}-\tilde{Q}^{2n}}{\tilde{P}^{2n+2}+\tilde{Q}^{2n+2}}e^{jkz}\mathrm{d}k,} \tag{2.112}$$

$$\boxed{\psi^y(\phi,z) = j\frac{1}{\pi^2}\sum_{n=0}^{\infty}(-1)^{n+1}\sin\left[(2n+2)\phi\right]\int_{k=-\infty}^{\infty}\frac{1}{k}\frac{\tilde{G}_y^1(k)T(k)}{\tilde{P}^2+\tilde{Q}^2}\prod_{m=0}^{n}\frac{\tilde{P}^{2n}-\tilde{Q}^{2n}}{\tilde{P}^{2n+2}+\tilde{Q}^{2n+2}}e^{jkz}\mathrm{d}k,} \tag{2.113}$$

$$\boxed{\psi^z(\phi,z) = \frac{1}{2\pi^2}\sum_{n=0}^{\infty}(-1)^{n+1}\cos\left[(2n+1)\phi\right]\int_{k=-\infty}^{\infty}\frac{1}{k}\frac{\tilde{G}_z^0(k)T(k)}{\tilde{P}^1+\tilde{Q}^1}\prod_{m=0}^{n}\frac{\tilde{P}^{2m-1}-\tilde{Q}^{2m-1}}{\tilde{P}^{2m+1}+\tilde{Q}^{2m+1}}e^{jkz}\mathrm{d}k.} \tag{2.114}$$

Table 2.1: Equations corresponding to the main mode

Gradient	Surface current density	Stream function
x	$J^x_{s:\phi} = -j\frac{bg_x}{\pi a\mu_0}\cos(2\phi)\int_{k=-\infty}^{\infty}\frac{\tilde{\Gamma}_{xy}(k)T(k)}{\frac{\lvert k\rvert}{k}K_2'(\lvert k\rvert a)\left[\lvert k\rvert I_2'(\lvert k\rvert b)+\frac{2}{b}I_2(\lvert k\rvert b)\right]}e^{jkz}\mathrm{d}k$ $J^x_{s:z} = -\frac{2bg_x}{\pi a^2\mu_0}\sin(2\phi)\int_{k=-\infty}^{\infty}\frac{\tilde{\Gamma}_{xy}(k)T(k)}{\lvert k\rvert K_2'(\lvert k\rvert a)\left[\lvert k\rvert I_2'(\lvert k\rvert b)+\frac{2}{b}I_2(\lvert k\rvert b)\right]}e^{jkz}\mathrm{d}k$	$\psi^x = -\frac{bg_x}{\pi a\mu_0}\cos(2\phi)\int_{k=-\infty}^{\infty}\frac{\tilde{\Gamma}_{xy}(k)T(k)}{\lvert k\rvert K_2'(\lvert k\rvert a)\left[\lvert k\rvert I_2'(\lvert k\rvert b)+\frac{2}{b}I_2(\lvert k\rvert b)\right]}e^{jkz}\mathrm{d}k$
y	$J^y_{s:\phi} = -j\frac{bg_y}{\pi a\mu_0}\sin(2\phi)\int_{k=-\infty}^{\infty}\frac{\tilde{\Gamma}_{xy}(k)T(k)}{\frac{\lvert k\rvert}{k}K_2'(\lvert k\rvert a)\left[\lvert k\rvert I_2'(\lvert k\rvert b)+\frac{2}{b}I_2(\lvert k\rvert b)\right]}e^{jkz}\mathrm{d}k$ $J^y_{s:z} = \frac{2bg_y}{\pi a^2\mu_0}\cos(2\phi)\int_{k=-\infty}^{\infty}\frac{\tilde{\Gamma}_{xy}(k)T(k)}{\lvert k\rvert K_2'(\lvert k\rvert a)\left[\lvert k\rvert I_2'(\lvert k\rvert b)+\frac{2}{b}I_2(\lvert k\rvert b)\right]}e^{jkz}\mathrm{d}k$	$\psi^y = -\frac{bg_y}{\pi a\mu_0}\sin(2\phi)\int_{k=-\infty}^{\infty}\frac{\tilde{\Gamma}_{xy}(k)T(k)}{\lvert k\rvert K_2'(\lvert k\rvert a)\left[\lvert k\rvert I_2'(\lvert k\rvert b)+\frac{2}{b}I_2(\lvert k\rvert b)\right]}e^{jkz}\mathrm{d}k$
z	$J^z_{s:\phi} = -j\frac{g_z}{\pi a\mu_0}\cos(\phi)\int_{k=-\infty}^{\infty}\frac{\tilde{\Gamma}_z(k)T(k)}{\frac{\lvert k\rvert}{k}K_1'(\lvert k\rvert a)\left[\lvert k\rvert I_1'(\lvert k\rvert b)+\frac{1}{b}I_1(\lvert k\rvert b)\right]}e^{jkz}\mathrm{d}k$ $J^z_{s:z} = -\frac{g_z}{\pi a^2\mu_0}\sin(\phi)\int_{k=-\infty}^{\infty}\frac{\tilde{\Gamma}_z(k)T(k)}{\lvert k\rvert K_1'(\lvert k\rvert a)\left[\lvert k\rvert I_1'(\lvert k\rvert b)+\frac{1}{b}I_1(\lvert k\rvert b)\right]}e^{jkz}\mathrm{d}k$	$\psi^z = -\frac{g_z}{\pi a\mu_0}\cos(\phi)\int_{k=-\infty}^{\infty}\frac{\tilde{\Gamma}_z(k)T(k)}{\lvert k\rvert K_1'(\lvert k\rvert a)\left[\lvert k\rvert I_1'(\lvert k\rvert b)+\frac{1}{b}I_1(\lvert k\rvert b)\right]}e^{jkz}\mathrm{d}k$

3
IMPLEMENTATION

In this chapter the implementation of the target field method will be discussed. This is everything from computing the stream functions to building the physical coil. MATLAB® R2018b (MathWorks, inc.) is used to compute the stream functions found in the previous chapter. The possibilities and limitations of the numerical model are discussed in Section 3.1. The magnetostatic solver in CST Studio Suite® (Darmstadt, Germany) is then used to simulate the computed coils. The target field method is verified and the performance of the gradient coils is discussed in Section 3.2. The design, construction process and validation of the z-gradient coil is treated in Section 3.3. In Section 3.4 recommendations are made with respect to the designs of the gradient coils for the low field system.

3.1. MODEL UTILIZATION

In order for the inverse Fourier transform of the stream functions (Equations 2.112, 2.113 and 2.114) to converge apodization is required. This filters out the higher order modes when computing these equations. Therefore only the main modes of the stream functions as shown in Table 2.1 are considered in this chapter. This can be done without loss of generality.

In order to obtain physical feasible coils the desired length d should be chosen larger than a quarter of the radius. The target field cylinder radius (b) needs to be chosen smaller than a since the fields were considered in region I. All even integer values can be chosen for the parameter n. The apodization parameter h depends on the size of the coil and the resolution taken. Choosing $h = 0.1$ results in reasonable current values for the low field coil dimensions.

The stream functions are two-dimensional functions defined on the surface of a cylinder. The current paths are obtained by contour plotting the stream function and placing current paths in between these contour lines. The current amplitude is obtained by taking the difference in value of the neighbouring contours. The 2D patterns can be transformed to a 3D Cartesian coordinate representation. Figures 3.1, 3.2 and 3.3 illustrate this for the three gradient coils. In this general case 5 contours per minimum/maximum are taken. The desired length d is chosen to be equal to a, the radius of the coils. The parameter n governing the sharpness of the target field in the z-direction is chosen to be 8. These parameters are selected to give a general impression of the gradient coils. The figures on the left show the normalized stream functions and the corresponding current paths. The black contours represent paths with counterclockwise currents as they are placed on yellow surfaces which are positive stream function values. The red contours represent paths with a clockwise current direction. The figures on the right show a 3D representation of the coils.

The coil patterns can directly be related to the stream functions. The target field functions Γ_z and Γ_{xy} determine the behavior in the z-direction. Γ_z is an odd function of z which creates an odd stream function in this direction. For the x- and y-gradient Γ_{xy} determines the z-direction behavior. This is an even function resulting in even stream functions. The middle loop creates the desired field. The outer two loops correspond to the side-lobes of Γ_{xy}. The sine and cosine terms create the ϕ behavior. Two loops can be distinguished for the z-gradient due to the $\cos(\phi)$ term. Four loops can be distinguished for the x- and y-gradients corresponding to the $\cos(2\phi)$ and $\sin(2\phi)$ terms. The only difference between the x- and y-gradient is the 90 degree shift in the ϕ-direction.

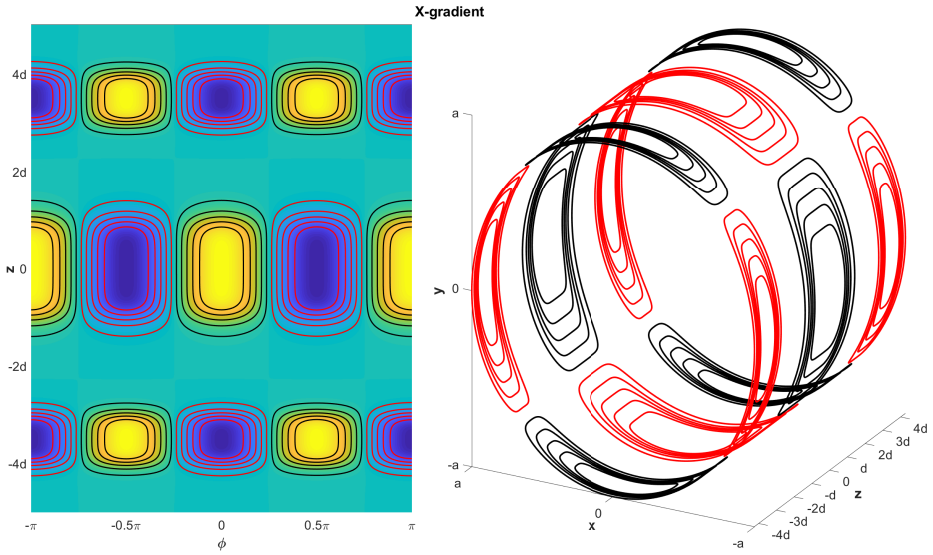

Figure 3.1: The left figure shows the normalized stream function and corresponding current paths of the x-gradient. Yellow corresponds to positive stream function values, blue to negative. The right figure is the 3D representation of the left figure. Black corresponds to counterclockwise red to clockwise.

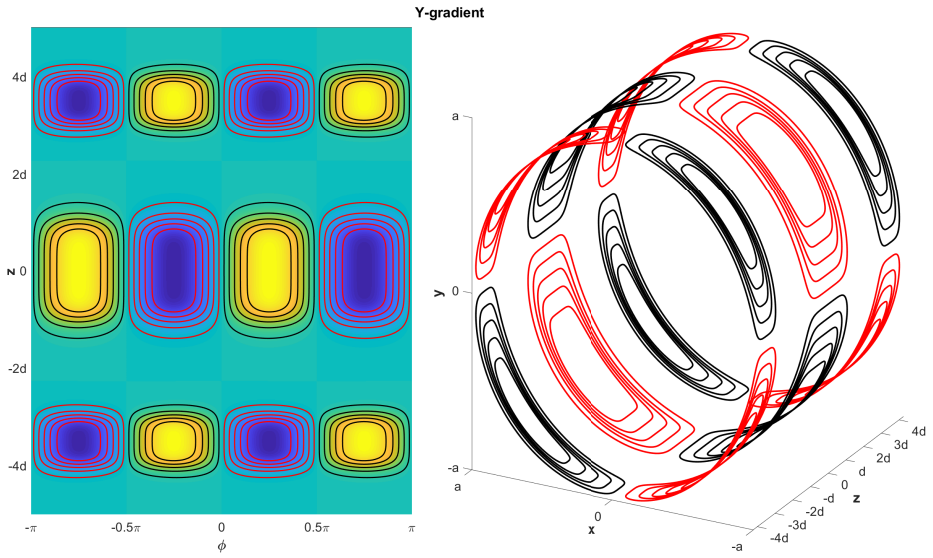

Figure 3.2: Showing the same as the figure above but for the y-gradient.

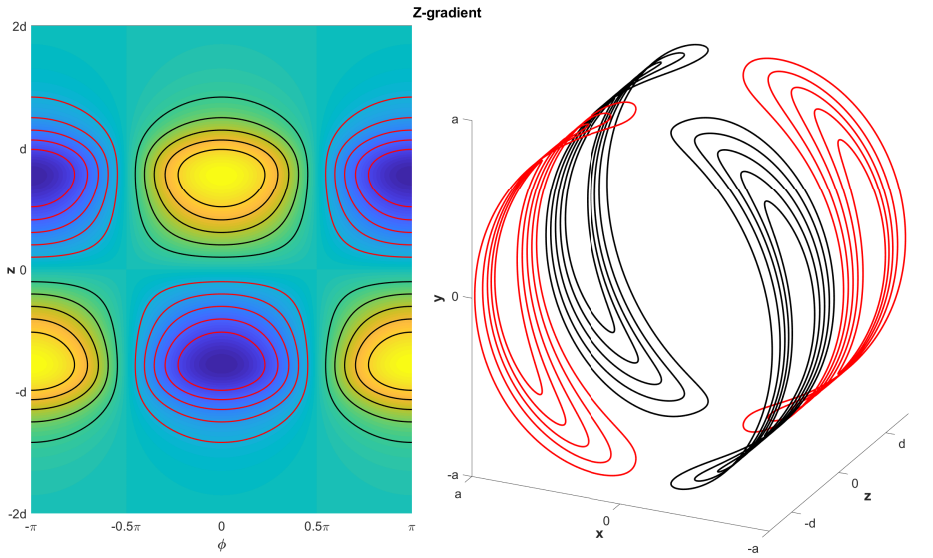

Figure 3.3: Showing the same as the figures above but for the z-gradient.

The length of the gradient coil is an important constraint for the low field system. This length can be influenced by changing certain parameters. Starting with the z-gradient: Increasing the desired length parameter d stretches the coil in the z-direction as is to be expected. Figure 3.3 shows that for a target field of desired length d the coil realization is about $3.5d$. This minimum length can be decreased by increasing the parameter n. A sharper target field is then prescribed resulting in denser wire patterns at the edges of the coil. This is the result of the higher current density required to obtain the target field. Figure 3.4 shows the z-gradient coils when taking different values for n. The right-hand side of Figure 3.4 shows a coil where $n = 26$, this squeezes the coil to a length of approximately $2.5d$. A disadvantage of creating a shorter coil is that the current required for a specific field strength increases. The turns at the edges of the coil are in opposite direction. These are now closer to the imaging volume and will subsequently decrease the target field values. The difference in required current between $n = 6$ and $n = 26$ is approximately 20% more. For the x- and y-gradient coil n can also

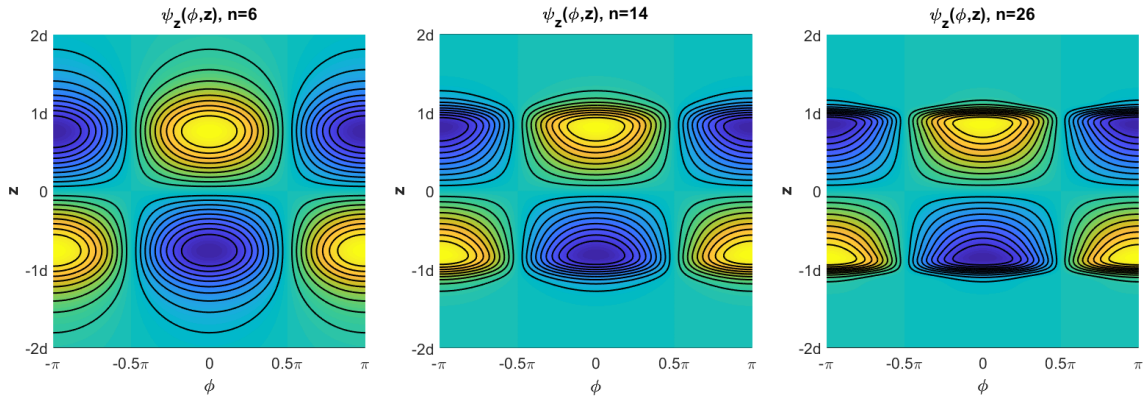

Figure 3.4: The difference in coil lengths caused by changing the target field parameter n.

be increased to shorten the coil. Here the required current is not influenced by n. This is due to the change in wire pattern not being in the direction of the linear behavior. For all three coils increasing the number of streamlines will result in more dense wire patterns and also slightly increase the length of the coil. In general it can be said that a coil with a length larger than $2.25d$ can physically be built.

Implementing the stream functions into MATLAB® and extracting the contours results in a visual representation of the gradient coils. The stream functions can be related to the coils and the coil structures adjust as expected to changes in the target field. In the next section CST® will be used to verify the target field model.

3.2. CST SIMULATIONS

The design software CST® is controlled with MATLAB® using visual basic commands[20]. An interface between the two is created which automatically builds the coils in CST® using the coordinates supplied by MATLAB®. This allows fast simulations of different structures. The influence of changing certain variables is then easily tested. The interface is a powerful tool for the gradient coil design.

For the simulations a magneto-static solver is used. The same current is applied to all paths separately. This is equivalent to connecting the current paths in series. When building the coil the paths connecting the adjacent current loops will be created in such a way that they cancel as much as possible. This makes the simulation of separate contours realistic. Simulations including connecting paths were also done, but this did not lead to observable differences. The boundary is a perfect electric conducting (PEC) box placed at a distance of 15cm around the coil. This represents the Faraday cage of the low field system.

VALIDATION OF THE MODEL

The three gradient coils from Figures 3.1, 3.2 and 3.3 are converted to CST and a 3D field map is obtained for the three gradient coils. Figure 3.5 can be used to clarify which planes are considered. Figure 3.6 shows a surface plot of the x-component of the magnetic flux density. These figures correspond to the x- and z-gradient coils. The y-gradient is equivalent to the x-gradient but rotated 45 degrees and is for that purpose left out. The intensity plot shows that the colors change gradually with position as is expected from the desired

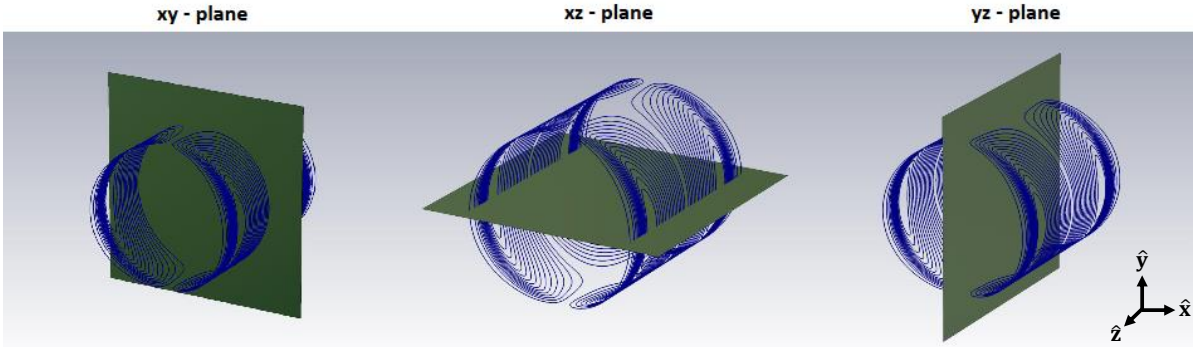

Figure 3.5: The z-gradient coil with the different planes that are distinguished.

linear behavior. In order to verify the model the simulated fields will be compared to the target fields. The target field is prescribed on a cylinder with radius $b = 0.5a$. The simulated field values on a line in the z-direction on this cylinder are displayed. This should result in $\Gamma_{xy}(z)$ for the x-gradient and $\Gamma_z(z)$ for the z-gradient. Normalized plots of the simulated and target field are shown in the top of Figure 3.7. The simulated fields are in reasonable agreement with the prescribed target fields and appear to be smoothed versions of it. This is due to the apodization. Another important result is obtained when removing the outer loops of the x- and y-gradient positioned at˜$\pm 4d$. This is done after computing the stream functions and obtaining a value for the current. The resulting simulated field taken on a line on the cylinder in the z-direction is shown with the black dotted line in the top right figure. The desired part of the target field is still obtained. This means the gradient coil can be made shorter after a value for the current is obtained. To confirm the behavior in the ϕ-direction the field values are taken on a line around the cylinder. For the x- and y-gradient this should result in a sine and cosine respectively. For the z-gradient the amplitude should be constant. The bottom plots in Figure 3.7 show that this desired behavior is obtained for the x- and y-gradient. For the z-gradient there is a small ripple. This is caused by the fields in the xy-plane which are shaped oval, due to the geometry of the coil.

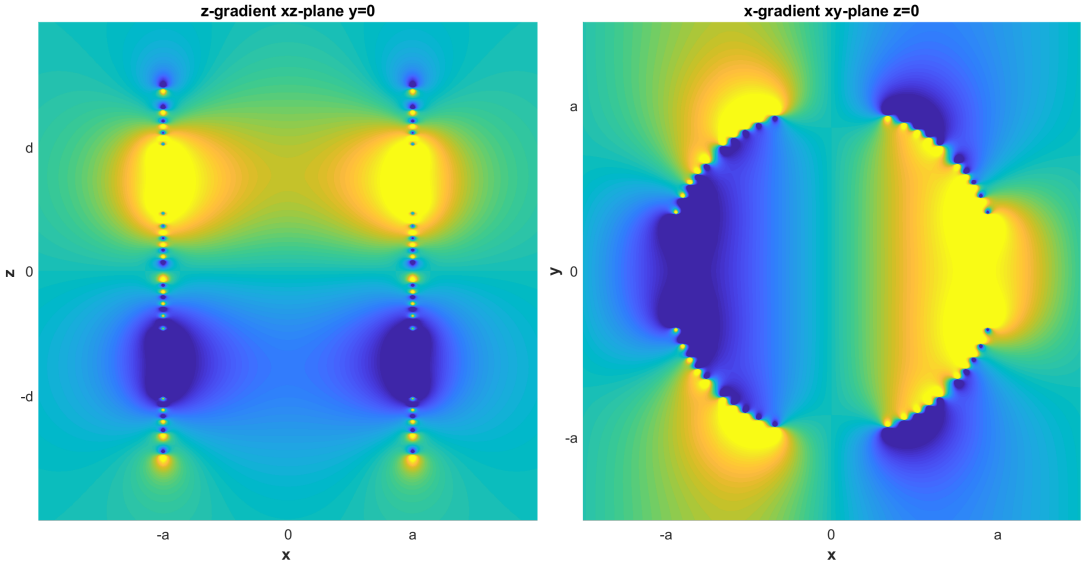

Figure 3.6: CST simulation results for z-gradient (left), the x- (right). The figures are intensity plots of the x-component of the magnetic flux density. Yellow represents positive, blue negative field values.

Table 3.1: Efficiency of the size normalized gradient coils fed with 1A of current and 5 turns per minimum/maximum. The second column shows the efficiency η. The third column the total length l of the current paths for five turns per quadrant. The last column shows η divided by the total length l. The side loops of the x- and y-gradient coil were not considered in these calculations.

Gradient	η [μT/m/A]	l [m]	η / l [μT/m^2/A]
z-gradient	4.16	128	0.0325
x/y-gradient	6.67	111	0.0601

The values of the current obtained from the model result in the prescribed target fields when fed into the simulated coils. With the z-gradient the current values are influenced by the apodization. For the x- and y-gradient the computed current values are not as susceptible to changing the apodization parameter h. This has to do with the linear behavior not being in the apodization direction. It was seen that changing n gives a different value for the current and in simulations it was confirmed that the field strength changes accordingly. When increasing n the target field pattern is more difficult to obtain due to the apodization filtering this sharp behavior. Choosing higher n is an adequate way to decrease the coil length, however one should not expect the sharp transitions in these target fields to be accurately obtained.

COIL PERFORMANCE

Now that the working of the model is confirmed the performance of the coils can be examined. In Figure 3.6 the same color scale is used for the surface plots. The simulations are done with the same number of turns per coil and are fed with a unit current. The figure indicates that the x-gradient coil generates a stronger field with the same current and number of turns with respect to the z-gradient. To obtain a measure for this the coil efficiencies will be compared. The gradient efficiency (η) is the amount of field that is produced with a unit current when the radius a = 1m and $d = a$. This measure is however dependent on the number of turns N. In order to correct for this the length of the current paths is calculated and η is divided by the total length. This results in an efficiency measure per unit length of coil. Table 3.1 shows these values for the different gradient coils. For the x- and y-gradient coil only the middle coils are taken into account. It can be observed that these coils perform significantly better than the z-gradient coil. The same gradient field strength can be obtained with less material. This will result in a lower resistance and inductance for the x- and y-gradient coils.

Another performance measure is the linear uniformity of the gradient field. The intensity plots in Figure 3.6 show that the field is not uniformly linear throughout the desired region. When considering the field values on lines in the corresponding coil direction the field should vary linearly. Taking different lines in the same direction within the desired region should result in the same field values. Figure 3.8 shows the field values on these lines for the two gradients. It becomes clear that the z-gradient behaves poorly with respect to the x-gradient which shows almost no deviation from the central line. Another thing to observe is that the linear regions for the x- and y-gradients extend to the bore of the gradient. The peaks shown in the left figure correspond to the radius of the coil being reached. For the z-gradient coil the prescribed linear region of d is obtained. Spatial encoding can be performed in a region of approximately $1.5d$.

Figures 3.9, 3.10 and 3.11 show the error with respect to the central line for the three planes. The values shown on the contours are percentages of this error. The red dotted line shows the central line from which the error is computed. The first thing to notice is that for all three planes the error contours are closer to the central line for the z-gradient. This makes the volume in which spatial encoding can be performed without distortions smaller. The left error plot of Figure 3.9 shows the error contours are oval. This corresponds to the small ripple found when taking values on a circular line around the target cylinder. The error plots are intrinsic to the coils. The x- and y-gradient have their linear behavior towards the coil they can thus make use of the spreading of the field further away from the coil. With the z-gradient coil this is not the case as the linear variation is along the bore. This problem is not easily solved, the field will always become larger moving towards the coil. When using slice select this is problematic as straight slices will not be excited. With 3D imaging it is expected that this problem can be partially solved in a post processing step for a known gradient field due to larger volumes being excited.

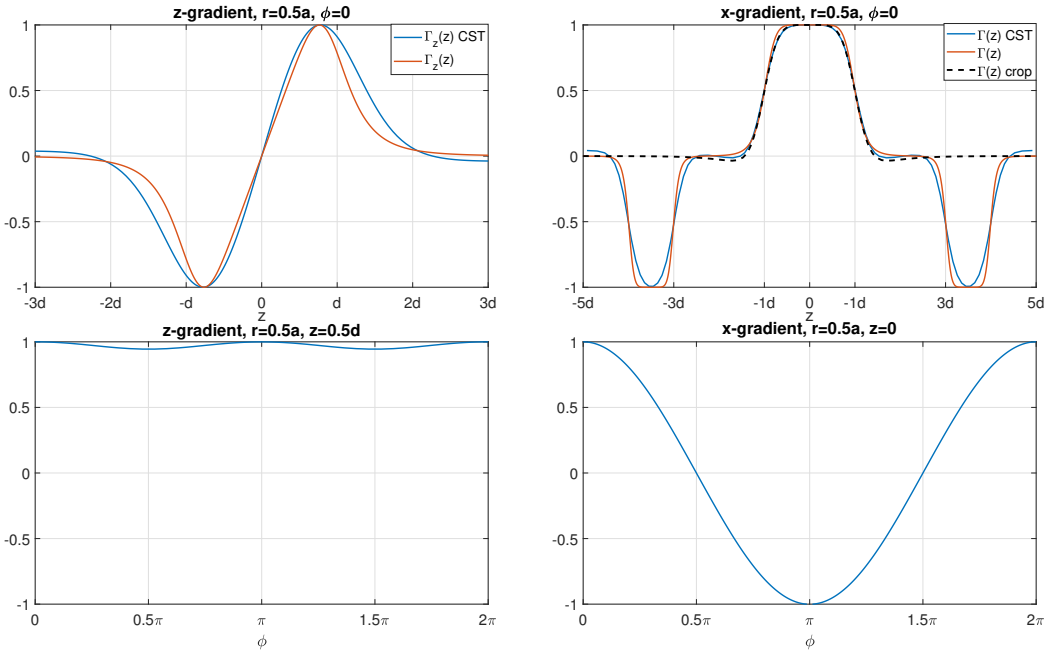

Figure 3.7: The verification of the target field model with the CST simulations. The top figures show the simulated (blue) and prescribed (red) Γ_z and Γ_{xy} respectively. Furthermore, the dotted line in the top right figure shows the field values for the x-gradient coil when only the center coil is taken into account. The lower figures display the simulated field values taken on a line around the target field cylinder. This should result in flat behavior for the left figure and a cosine for the right figure.

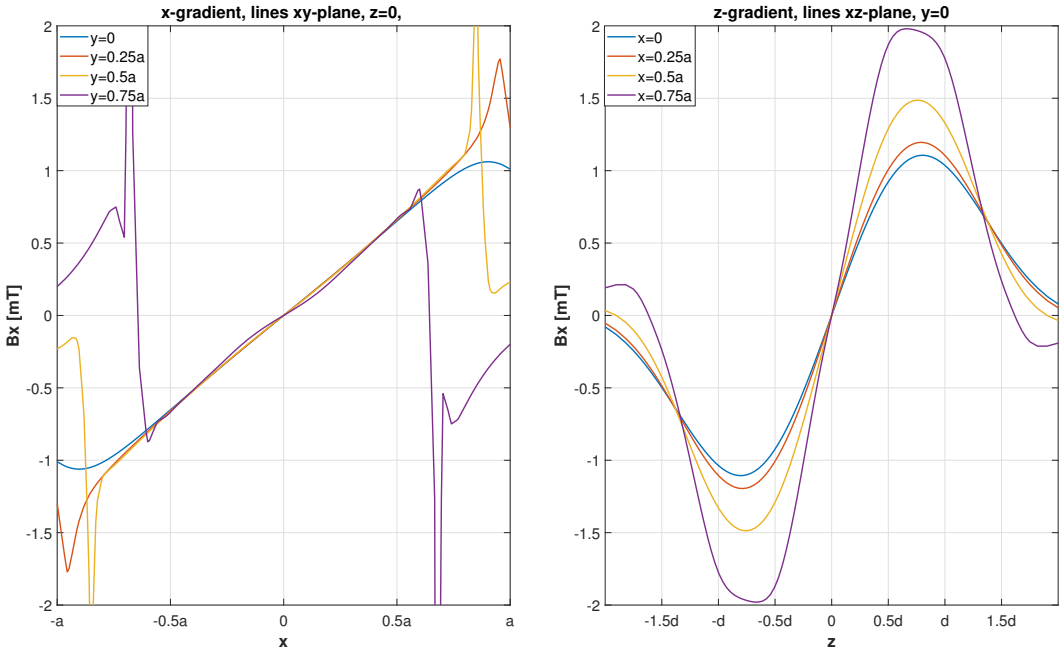

Figure 3.8: Field values taken on lines for the two gradient coils. The lines are taken in the direction of the linear behavior.

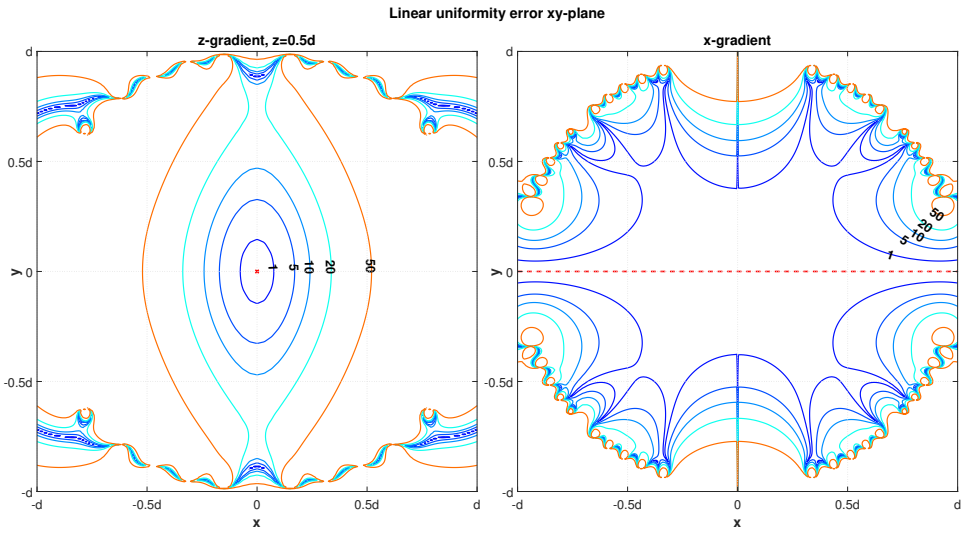

Figure 3.9: Contour plots of the linear uniformity error in the xy-plane. The error is calculated with respect to the central linear line. For the x-gradient this is the line with y=0,z=0. For the z-gradient the line x=0,y=0 is taken. The red cross or dotted line shows this line. The error is shown in percentage on the contours.

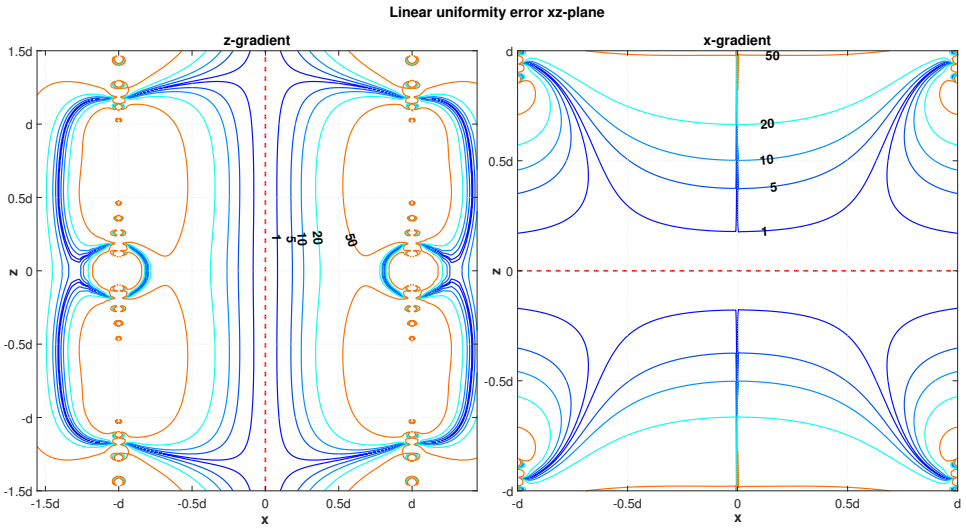

Figure 3.10: Error plots as described above but taken for the xz-plane.

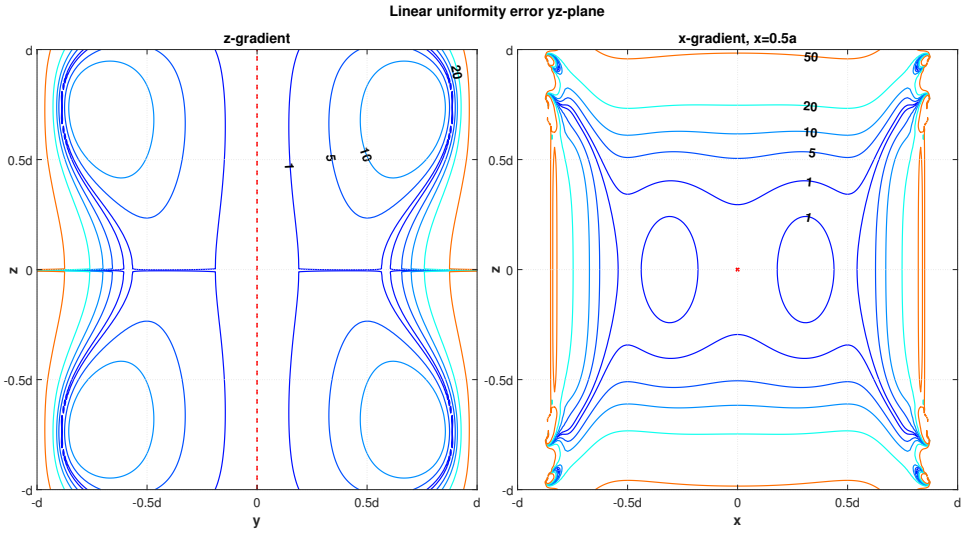

Figure 3.11: Error plots as described for the top figure but for the yz-plane.

3.3. GRADIENT COIL CONSTRUCTION

A Prototype of the z-gradient coil is constructed. This is the most difficult coil with respect to performance and wire pattern. Due to this the coil is chosen to be the one closest to the imaging volume. The goal is to design a coil that can be implemented into the low field system as described before. This physical verification is important in order to know how well the CST simulation resembles reality and what challenges arise when building a gradient coil for this low resource setting.

Due to the physical dimensions of the low field magnet the gradient coil can have a maximum length of 350mm. A desired linear region of 150mm in the z-direction is requested as this region is long enough to image a brain. The three gradient coils can have a maximum combined thickness of 20mm. The simulation results show that it is possible to create a coil with these dimensions. However it will be pushing the target field method to its limits.

Without changing the dimensions of the coil the field strength can be increased by increasing the driving current (I) and the amount of turns. The power scales with I^2 and the inductance increases when adding more turns. The imaging sequences which the gradients are meant for do not require fast switching of the fields. Having a small inductance is thus of less importance. Limiting power dissipation is more urgent because the heating of the gradients can influence the magnetic field exerted by the permanent magnets. In addition, low power requirements are preferable in a low resource setting. For this reason 14 turns are chosen. This amount fits on the coils without adjacent turns overlapping. In order for the wires to fit on the cylinder the design parameter n is chosen to be 26. The required field strength is set to 10mT/m. The model states that approximately 30A is needed to obtain the required field strength, but only 10A is available as a driving current. Three layers are thus required in order to reach the target field strength. The resulting simulated coil can be seen in Figure 3.12. The figure shows that the wires are indeed closely spaced near the edges of the coil in order to obtain the requested performance.

The conducting paths can be synthesized using different materials and techniques. Wires or a conducting sheet is used in most cases. For wires, a gradient coil can be hand wound using solid copper wire. A mold in which the wires can be placed in combination with epoxy or an equivalent bond can be used to keep the wires in place. When constructing a coil out of a sheet of copper the streamlines can be cut out. This results in conducting tracks between streamlines which vary in width. The patterns can for instance be cut out using a waterjet-cutter or a milling machine. The coordinates of the streamlines can be programmed into these machines creating a very accurate representation of the patterns. The sheet can then be bent around a cylinder resulting in the gradient coil.

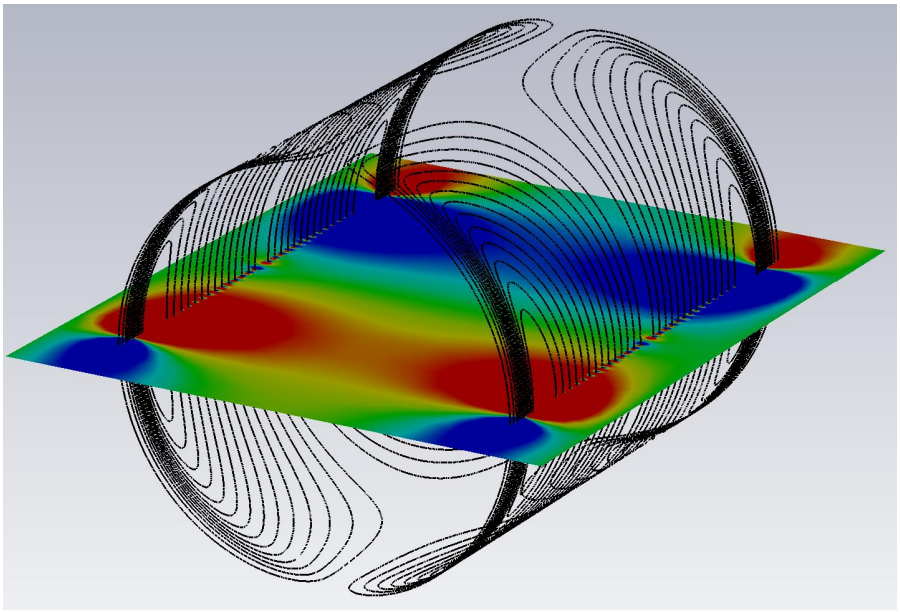

Figure 3.12: The z-gradient coil simulated in CST. This is the coil that is physically built. The intensity plot of the magnetic flux density in the xz-plane is also shown as an illustration.

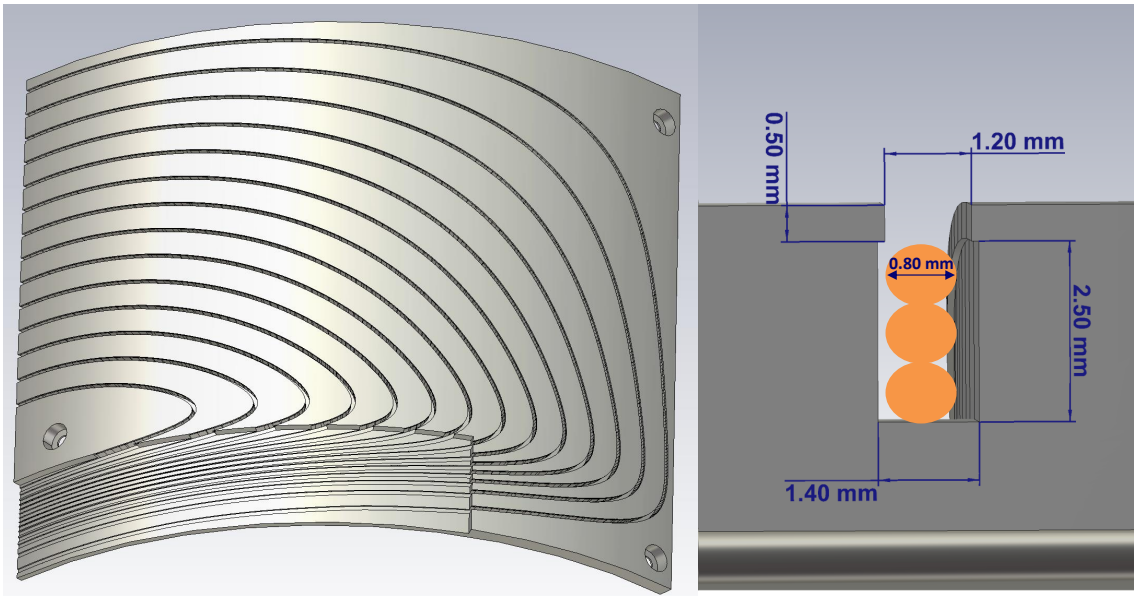

Figure 3.13: The left figure illustrates the schematic of the mold which will hold the wires. This is one eighth of the gradient coil. The right figure shows the profile of the slots which will fit three wires on top of each other. The dimensions of the slot are also given in the figure.

Both techniques have their benefits. Cutting out a sheet is how the state of the art gradient coils are constructed. A larger surface area is exploited decreasing the resistance and consequently the power requirement and joule heating. However the machines used in this process are expensive and are unlikely to be available in a low resource setting. For a prototype a hand wound design using wire may be more appropriate. Due to the small bore the power consumption weighs less heavy than for instance with conventional MRI bore sizes. Also the low available current will require multiple layers and shielded wires can be placed directly on top of each other. Furthermore, everything can be made in house and the materials and process are less expensive. Lastly The structural strength is expected to be better with the wire model due to the molds holding the wires. The choice was therefore made to use wires. Copper wire with a diameter of 0.8mm is chosen as it is easily manipulated.

Accurate positioning of the wires is important to acquire the correct target field. The switching of the field creates forces on the wires which can cause the wire to be displaced. In order to deal with this a 3D printed mold is designed which holds the wires in place and ensures correct positioning. The molds are created in CST by extruding the current paths into a flat surface. Figure 3.13 shows a schematic of this mold. At the edges of the coil the margin between the wires is too small to create a wall between them. Moreover, a connection to the other paths needs to be made. For this purpose a rectangle is extruded in this area. The right-hand side of Figure 3.13 shows a schematic of the slots, three wires can fit on top of each other. The slots are more narrow at the top creating a click mechanism. Due to the light flexibility of the PLA printing material this works very nicely, the wires can be pressed in and will stay put. The appropriate dimensions of the slots were found by making a prototype with different slot sizes. Additional glue is used as a safety precaution. The mold has a height of 5mm making it possible to fit another two coils around the prototype in a later stage. Various printing techniques, printers and materials were considered. The best printing technique was found to be on the back with support underneath the print. The Ultimaker 3 extended 3D printer created the best quality prints. One print would take 1.5 days to complete. It was found that the quality of the slots and the resulting click mechanism is important in order to ease construction. The molds resulting from different printing techniques are shown in the left of of Figure 3.14.

The molds are positioned on a plexiglas cylinder with a diameter of 270mm. The wire is then placed inside the slots. Approximately 120m of wire was required. This corresponded to the current path length calculated with MATLAB®. The construction took about 30 hours, this was mainly due to half the molds not having the click mechanism making the construction very difficult as wires tended to pop out of the mold. The material costs of the z-gradient coil were approximately €30 without the plexiglas cylinder. The resulting coil is shown in Figure 3.15.

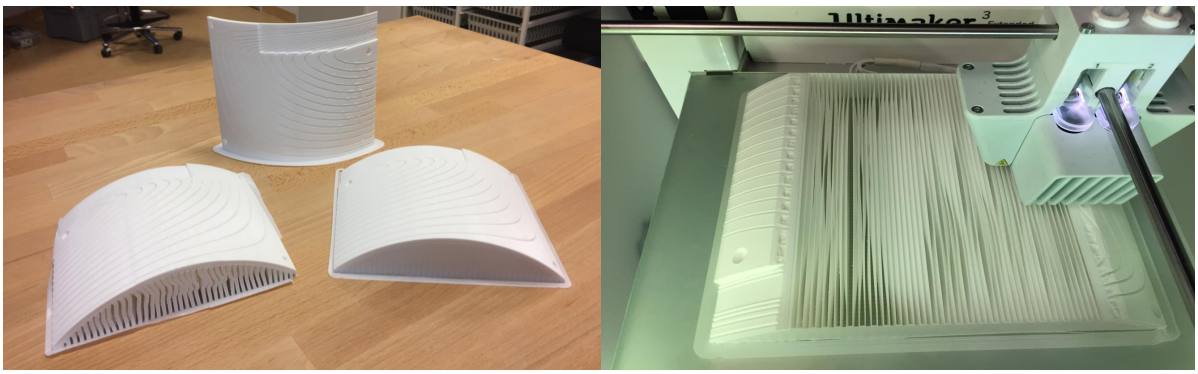

Figure 3.14: The left figure shows the resulting molds created with three types of printing techniques. The mold on the right laying on its back is the one with the best slots. The right figure shows the 3D printing process.

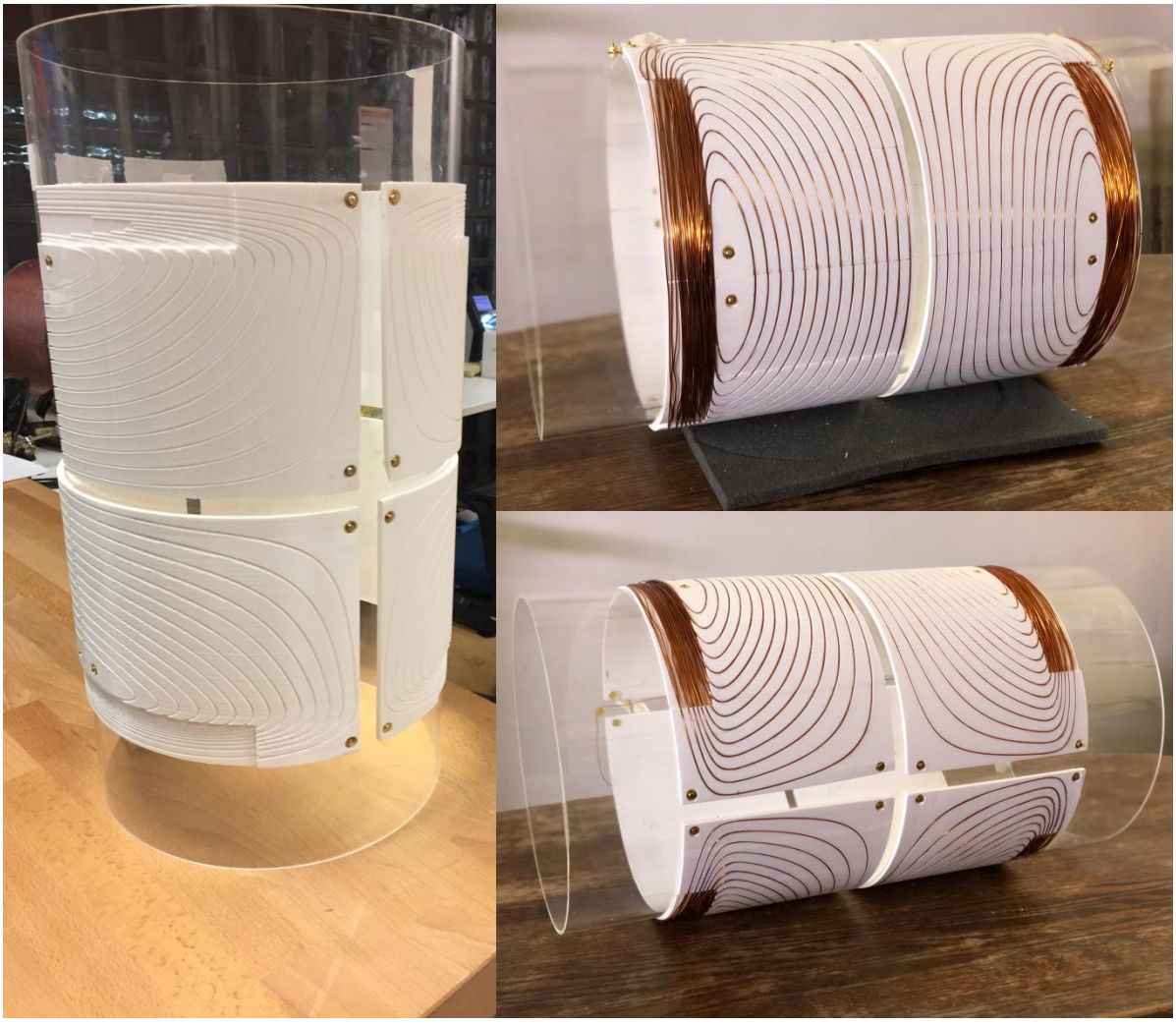

Figure 3.15: the left figure shows the molds mounted on the plexiglas cylinder. The right-hand side figures show the finished z-gradient coil from different angles.

TESTING AND RESULTS

The magnetic flux density of the prototype obtained in the simulations is compared with a field map created using a multipurpose 3-axis measuring robot [21]. An arm is mounted on the robot which can move through the bore of the gradient and can hold a field probe. The AlphaLab inc. Gauss meter model GM2 with a high stability probe is used to make the measurements [22]. The test setup is shown in Figure 3.16. The measured field has a diameter of 220mm, a length of 360mm at a resolution of 10x10x10mm. The coil is fed with a DC power supply which feeds the coil continuously with 2.1A of current. During the measurement the coil temperature stayed constant at 30°C. A background field map is created to correct for the fringe fields of the nearby MRI scanner and the undesired fields generated by the power supply. Creating a field map takes 6 hours.

Figures 3.17 and 3.18 show two slices of simulated field next to the measured field. It can be observed that the measured field closely corresponds to the simulated field. The field strength as well as the shape are in agreement with the simulations. Figure 3.19 shows the field values on a line through the middle of the bore for the target, simulated and measured fields. The CST simulations correspond very well to reality. The construction method can therefore be concluded to be accurate. The region where the field is linear is approximately 150mm, the region where spatial encoding can be applied is 200mm. Figure 3.19 shows two dips (at $z = -50$mm and $z = +60$mm) in the measured field values. This is suspected to be due to the supplied current drifting during the measurement. The locations of the artifacts correspond to the moments in time when this happened.

The resistance of the coil equals 3.86Ω. The inductance is measured to be 1.37mH. When running spin echo imaging sequences and feeding the coil with 10A the coil shows no heating. With a turbo spin echo sequence an insignificant amount of heating can be observed. These measurements were done in an open environment. Additional testing needs to be done when placing the coil in an area where airflow is confined.

The measured field of the constructed gradient coil corresponds to the simulated target field. The resistance and inductance of the coil are fairly high. A thicker wire diameter can be used to lower the resistance. The high value of the inductance can be attributed to the 3 layers of wire needed to supply the magnetic field strength. Layers can be taken off by increasing the driving current or lowering the requirement for gradient field strength. Relaxing the parameter n will also slightly decrease the required current. Using these lessons the following section holds the proposed designs of all of the gradient coils for the low field system. Also the conclusions of this chapter are drawn.

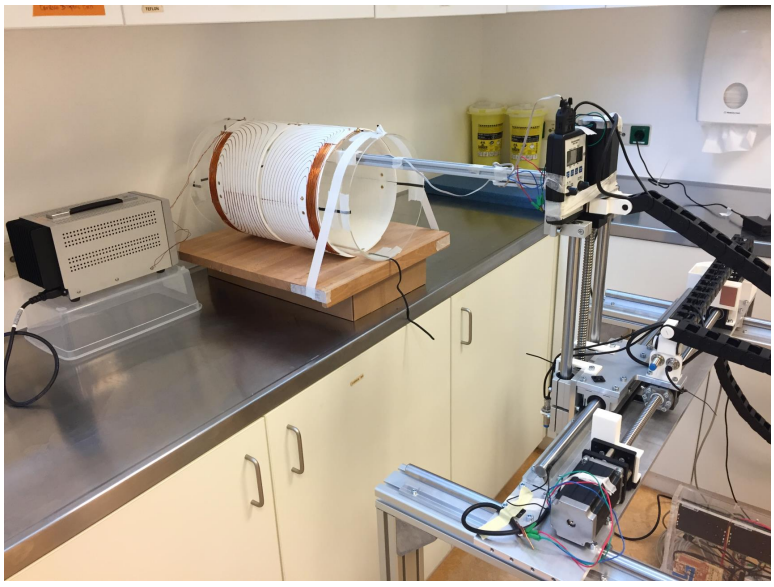

Figure 3.16: The test setup: The gradient coil is fed by the power supply which can be seen on the left. The robot arm with the Gaussmeter moves through the bore of the gradient coil mapping the field.

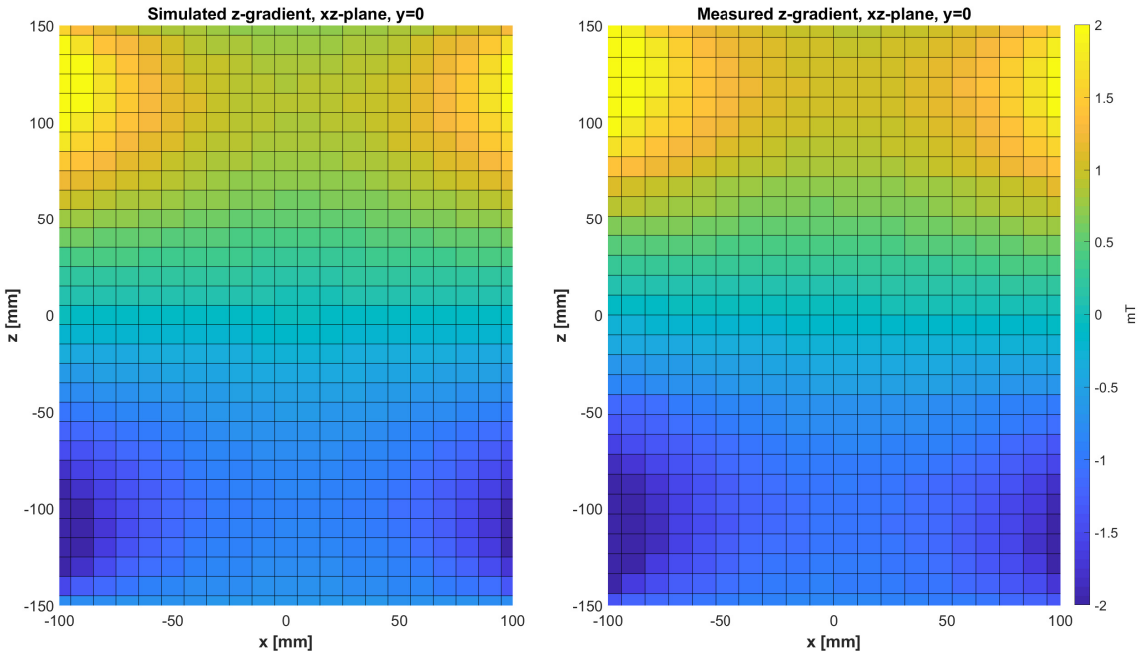

Figure 3.17: Surface plots of the simulated (left) and measured (right) z-gradient coil data. The middle slice of the xz-plane is displayed.

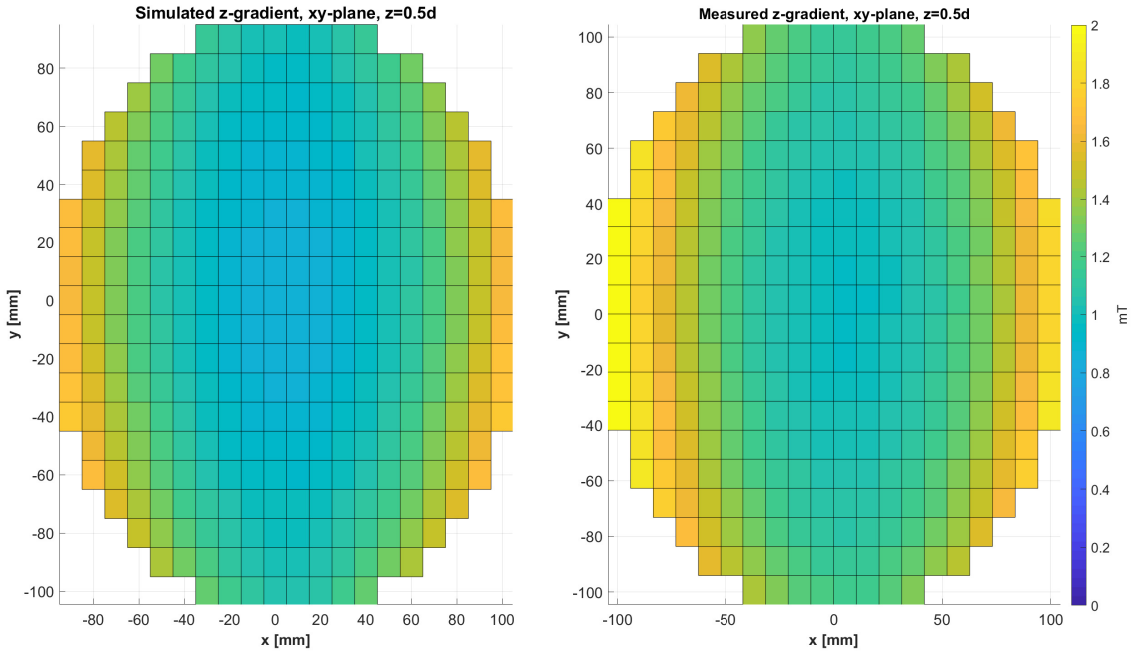

Figure 3.18: Surface plots of the simulated (left) and measured (right) z-gradient coil data. A slice at $z = 0.5d$ in the xy-plane is displayed.

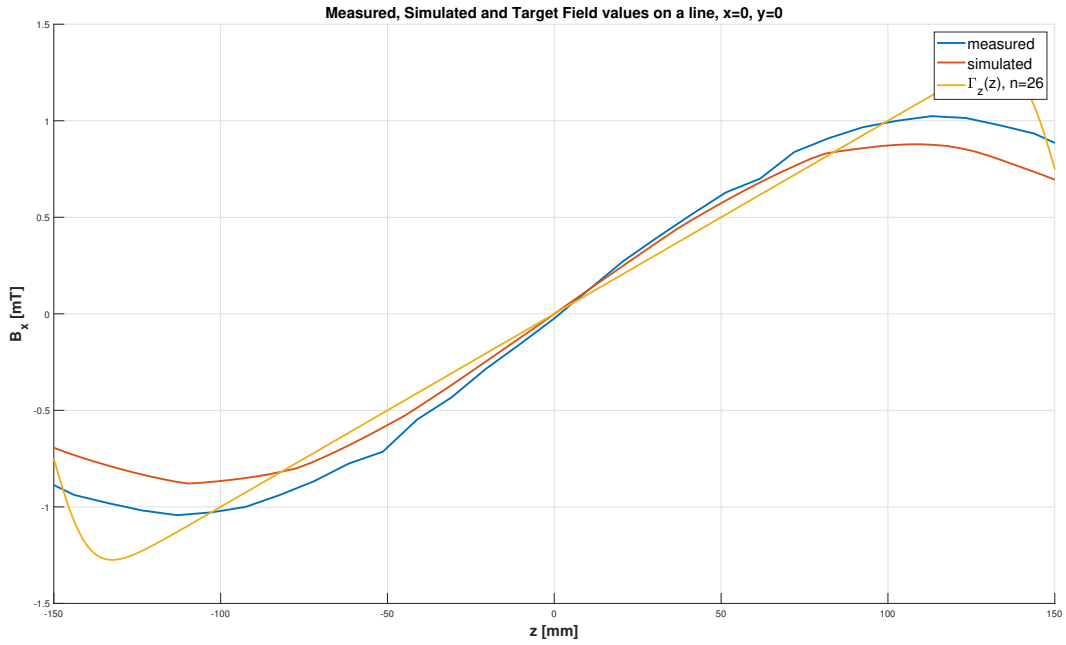

Figure 3.19: Field values on a line through the center of the bore of the measured, simulated and target field. The dips in the measured field at z=-50 and z=+60 are likely to be due to drift in the power supply.

3.4. CONCLUSIONS AND RECOMMENDED DESIGNS

The implementation of the target field equations in combination with the direct link to the simulation tool is shown to be a powerful method for gradient coil design. The implemented target field model was verified to create the target fields. We observed that the x- and y-gradient coils performed better with respect to linear uniformity and efficiency than the z-gradient coil. We built a prototype for the z-gradient coil and we can conclude that the construction technique created an accurate representation of the simulation results. The field maps obtained from CST® can thus also be used for post processing purposes. From the prototype it was found that both the inductance and the resistance can be improved. This resulted from the relatively low driving current of 10A that the coil was designed for. In addition, the wire diameter could have been chosen larger to decrease the resistance.

To create more design freedom the gradient amplifier is modified to supply a maximum of 30A with a load of 0.5Ω. Two layers are taken off creating a one layer design. This will significantly reduce the inductance, resistance and thickness of the coil. However due to the power dissipated being proportional to I^2 heating will become significant. To compensate for this a thick wire diameter of 1.5mm is chosen. Table 3.2 shows the wire length, resistance and power dissipation for the prototype and the proposed design using the same amount of turns. The table shows a reduction of power dissipation, resistance and wire length which will consequently decrease the inductance. The thicker wire is more difficult to bend making the construction by hand more

Table 3.2: Top row shows the length, resistance and required power for the prototype. The bottom row shows this for the proposed design when only changing the amount of layers and the wire thickness.

	l [m]	R [Ω]	P [W]
3 layers, 0.8mm wire , I=10	120	3.8	380 W
1 layers, 1.5mm wire, I=30	40	0.384	346 W

challenging. Moreover, the adjacent wires will overlap at the edges of the coil. By relaxing the desired region parameter d and the sharpness parameter n the required current decreases and the wires can fit next to each other. Decreasing n also makes the coil more efficient. Even with creasing d and n the region where spatial encoding can be applied can still be kept larger than 150mm. The chosen coil parameters and resulting

Table 3.3: The parameters and performance measures for the proposed gradient coils. The wire thickness chosen is 1.5mm.

Gradient	N	n	d [mm]	a [mm]	η [mT/A/m]	l [m]	$R[\Omega]$	P [W]
z-gradient	14	16	140	272/2	0.37	38	0.37	329
y-gradient	12	30	155	277/2	0.8	42	0.40	162
x-gradient	12	30	155	282/2	0.8	43	0.41	165

performance indicators are shown in Table 3.2. It can be observed that the expected power dissipation of the proposed coil is 15% less than the initial prototype. Furthermore, the material cost, thickness and the inductance is decreased. The Figures in the appendix show the simulation results and error plots for this specific coil. We can conclude that this coil can create a linear region of approximately 100mm and that spatial encoding can be applied in a region of 190mm. In a diameter spherical volume (DSV) of 100mm the linear uniformity error is already more than 20%.

The x- and y-gradient are more efficient. These coils are designed to create the desired field of 10mT/m using less than 20[A] resulting in less power dissipation. The parameters chosen are shown in Table 3.3. The parameters d and n are chosen high so that the flat region of Γ_{xy} is as large as possible and the adjacent wires nearly overlap at the edges of the coil. This does not influence the current required. Figures corresponding to these designs can be found in the Appendix. From these figures it can be concluded that a linear region of 200mm is easily obtained. Furthermore, both transverse coils have a linear uniformity error of approximately 5% in a DSV of 150mm

The simulation results turned out to be reproducible with the proposed construction method. It is advised that the next gradient coils are also constructed using this approach. The support printed underneath the mold made the 3D printing process slow. In the future we can experiment with printing flat molds that can be bent either by adding structural weaknesses or by heating the molds. Extra care needs to be taken with respect to the placement of the wires not being effected by the bending process. For the x- and y-gradient coil the printing of the molds is expected to be more efficient. The molds can easier be printed in sections. Also the prints use less surface area.

If the bore size were to increase power dissipation could become an issue. It is advised to investigate the construction using conducting sheets. It should be noted that skin effects and the capacitance between the sheet layers should be investigated prior to the construction. Alternatively the molds could also be made from plastic getting rid of the time consuming 3D print process. The coils then still need to be hand wound. It would be beneficial if the gradient coils could be extended in length in the z-direction. In a newer version of the magnet it is advised to leave room for longer gradients coils which could even extend the length of the magnet. The z-gradient coil efficiency can be increased with 20% by relaxing the parameter n. Additional turns would fit on the coil which would reducing the power requirement and make it more efficient. For the x- and y-gradient coils d could be increased to improve the linear uniformity region. In general we can conclude that increasing the length while keeping the requirements the same can decrease the inductance due to the current density being less concentrated.

4

CONCLUSION AND RECOMMENDATIONS

In this work we have shown how to design gradient coils for a Halbach permanent magnet system. The method described creates cylindrical gradient coils meant for a main magnetic field direction perpendicular to the bore. We have shown successfully that it was possible to use the target field method for the design of these gradients. The result was captured into one equation per gradient coil. We used the method to simulate and build gradient coils for the LUMC low field MRI system.

The first step in deriving the target field equations was finding a forward equation. This equation describes the magnetic flux density resulting from a certain current density. We found this by deriving the basic relations between the various magnetic field components and used the boundary conditions to introduce the current density. The magnetic field component was then composed from two cylindrical components.

To invert the forward equation the target fields were constrained to the surface of a cylinder. Furthermore, the gradient fields were defined in such a way that the Fourier analysis simplified to using only a few modes. Finally a Gaussian apodization function was introduced in order for the numerical Fourier transform to converge. Inverting the forward equation resulted in three sets of equations which described the current densities specific to the gradient coils. This showed us that it was possible to find the current densities corresponding to these specific field orientations using the target field approach.

Using stream function theory the current density was approached by discrete current paths. We showed that the wire patterns could be obtained by taking contours of the stream functions and placing paths between these contours. A value for the current was obtained by taking the difference in value between the neighbouring contours. This resulted in one stream function per gradient coil. Using MATLAB® we computed winding patterns corresponding to different target fields. The MATLAB® results showed us that the gradient coils resulting from the equations were physically realizable. Moreover, the winding patterns adapted accordingly to changes in the target field parameters.

An interface with the antenna simulation software CST® was created. With this tool simulated fields created by the gradient coils could be compared with the requested target fields. We observed that target fields were indeed produced by the gradient coils. The simulation tool also made it possible to obtain information on the performance of the coils. It was found that the coil which produced the gradient field along the bore performed poorly with respect to the others. The efficiency of the transverse coils was shown to be twice as high.

A prototype of the z-gradient coil was designed specifically for the low field system. From the simulation we found that the design specification could be met. However the length constraint in combination with the desired imaging region was not easily obtained. A longer coil would have been more efficient but unfortunately did not fit in the low field system. We then built the coil by hand winding copper wire into molds created with a 3D-printer. The gradient field of the constructed coil was mapped using a measuring robot. The field map that we obtained corresponded to the simulated fields. The measured inductance and resistance of this gradient coil were found to be too high. At the end of the thesis final designs were proposed resulting in three gradient coils that can be synthesized and should perform as desired for the low field system. Spatial encoding in a region of 210x210x150mm (x,y,z), is expected to be obtainable. With the x- and y-gradients the linear uniformity error is shown to be small in this region. For the z-gradient coil this error is larger and additional post-processing steps need to be taken in order to correct for this.

The following can be considered with respect to future work. The target field theory knows certain extensions which are used quite commonly in state of the art gradient coils. With the work presented in this thesis coils can be made that fit the requirements of the low field system. The minimum inductance extension would become useful when using imaging sequences that require fast switching gradient fields. The minimization of power will be required when moving to larger bore sizes.

Improvements with respect to the power efficiency and linear behavior inside the imaging volume can be obtained by creating longer gradient coils. Doing this can improve the efficiency of the z-gradient coil up to 20%. In addition, the field inside the imaging domain can be made more linear. For the x- and y-gradient coils the linear homogeneity can also be improved by creating a longer coil. Moreover, the inductance of the gradient coils is expected to be less due to the current density not being concentrated near the edges of the coil.

Temperature testing of the constructed gradient coil has been done on an elementary level. This gave a good indication with respect to the amount of heating. More tests in a confined area are however advisable. In the future the calculated power dissipation can then be used as a figure to indicate the amount of heating a coil will endure.

The influence and potential coupling of the designed gradient coils with the RF-receiver coil was not considered in this work. It could be that shielding between these two coil system is required in order for the coils not to interact with one and other.

Lastly we advise to investigate the construction of the gradient coils using conducting sheets. This can reduce the required power due to more surface area being used. Furthermore, these sheets can be mass produced, will take up less space and we expect the construction accuracy to be high. Eddy currents and the capacitive effects between the sheets needs to be investigated prior to the design of these type of coils.

Everything considered we believe we have created a design method that will bring the low field project one step closer to creating a fully working MRI system to detect hydrocephalus in Uganda.

A

SIMULATION RESULTS FINAL GRADIENT COIL DESIGNS

This appendix chapter holds the simulation results of the proposed gradient coils. These coils are designed for the low field system. The table below shows the parameters used during the simulations. This is followed by the figures showing the wire patterns, linear regions, surface plots and the linear uniformity error. This gives a total picture of the designed gradient coils.

Table A.1: The parameters and performance measures for the proposed gradient coils. The wire thickness chosen is 1.5mm.

Gradient	N	n	d [mm]	a [mm]	η [mT/A/m]	l [m]	$R[\Omega]$	P [W]
z-gradient	14	16	140	272/2	0.37	38	0.37	329
y-gradient	12	30	155	277/2	0.8	42	0.40	162
x-gradient	12	30	155	282/2	0.8	43	0.41	165

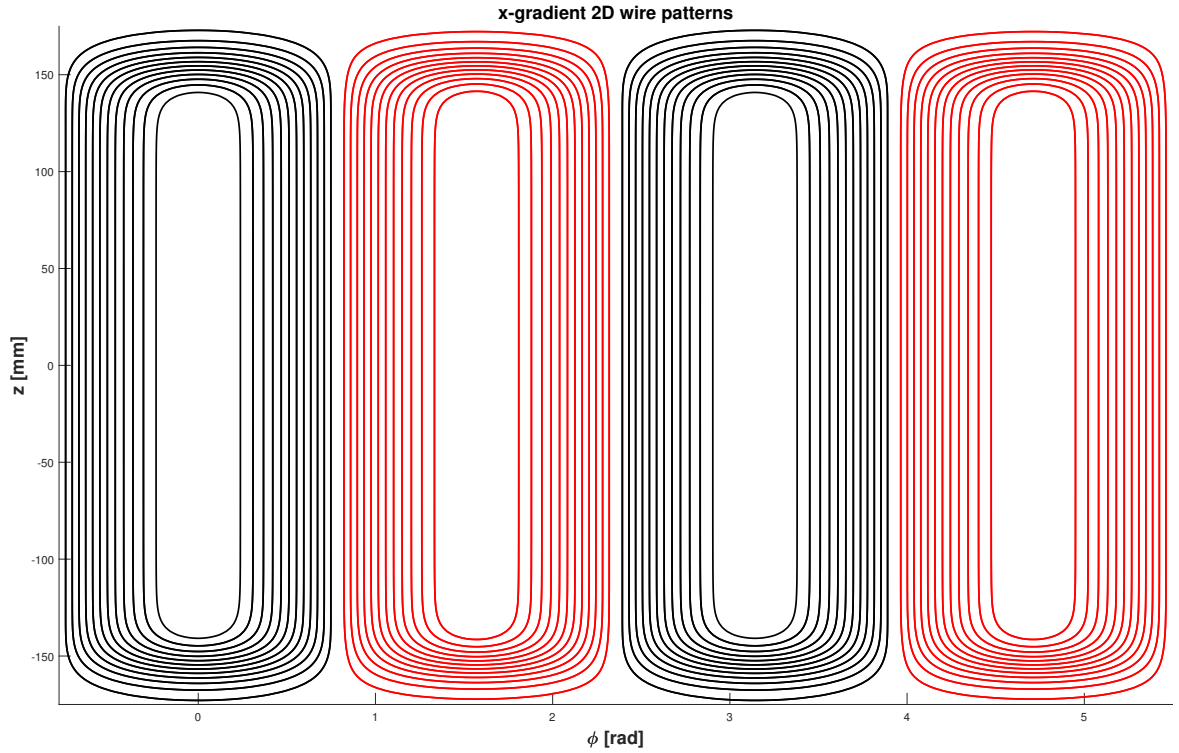

Figure A.1: Two dimensional view of the wire patterns for the x-gradient coil. Red contours correspond to a clockwise direction. Black contours the counterclockwise direction direction.

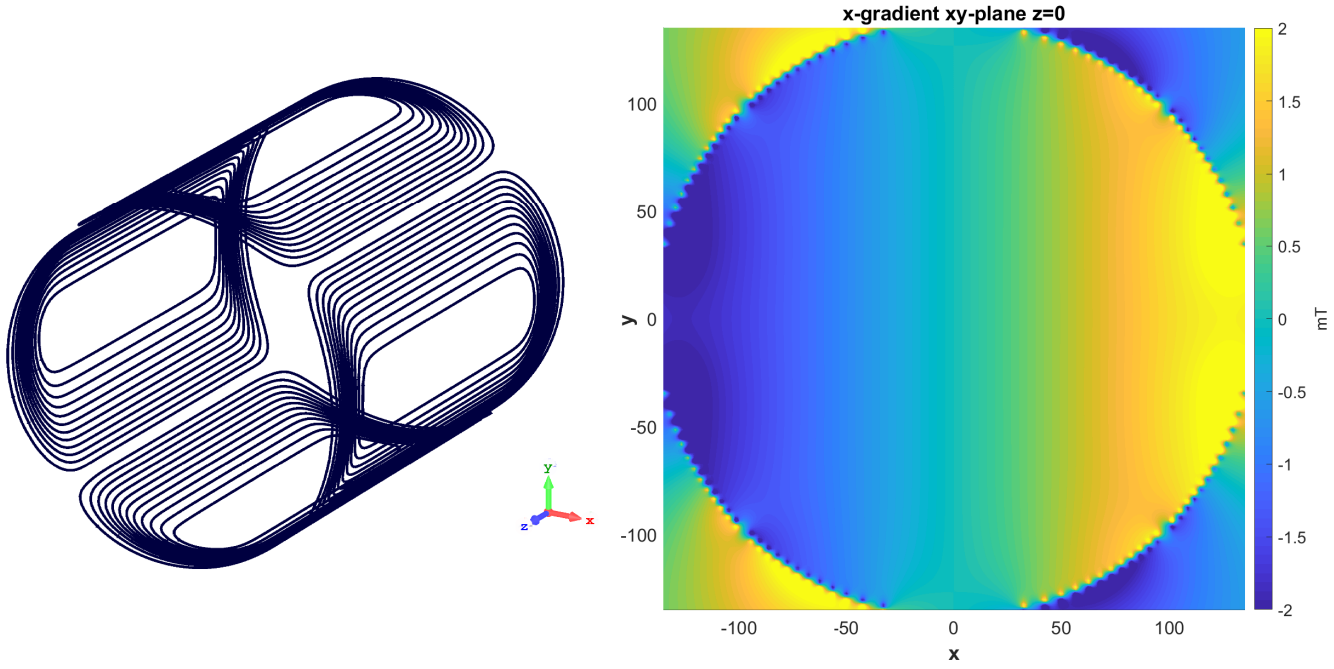

Figure A.2: Left 3D pattern of the x-gradient coil. Right the xy-plane surface plot.

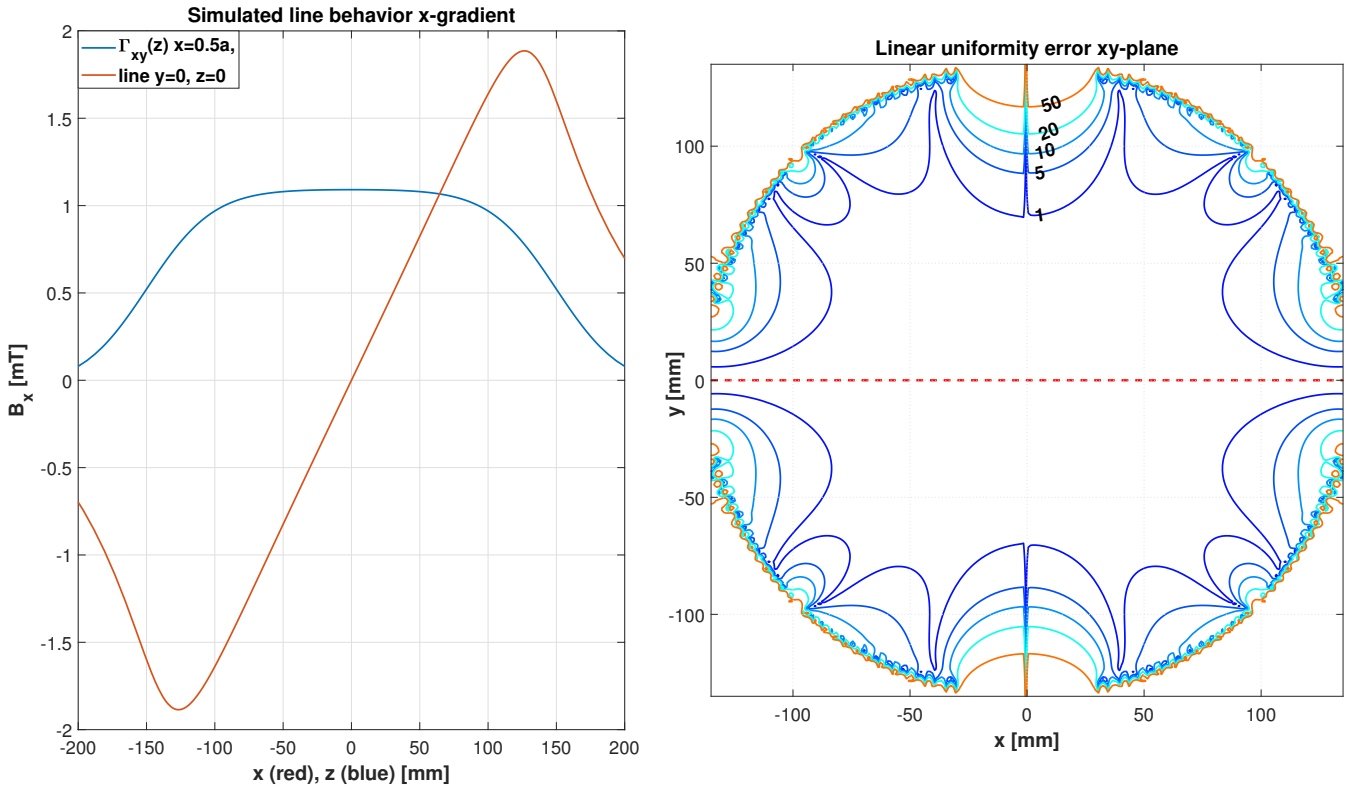

Figure A.3: left figure shows two lines, red shows the linear behavior when taking values on a the red dotted line shown in the right figure. The blue line shows the behavior along the bore axis. This gradient coil is fed with 20[A]. The right figure shows an error plot of the xy-plane.

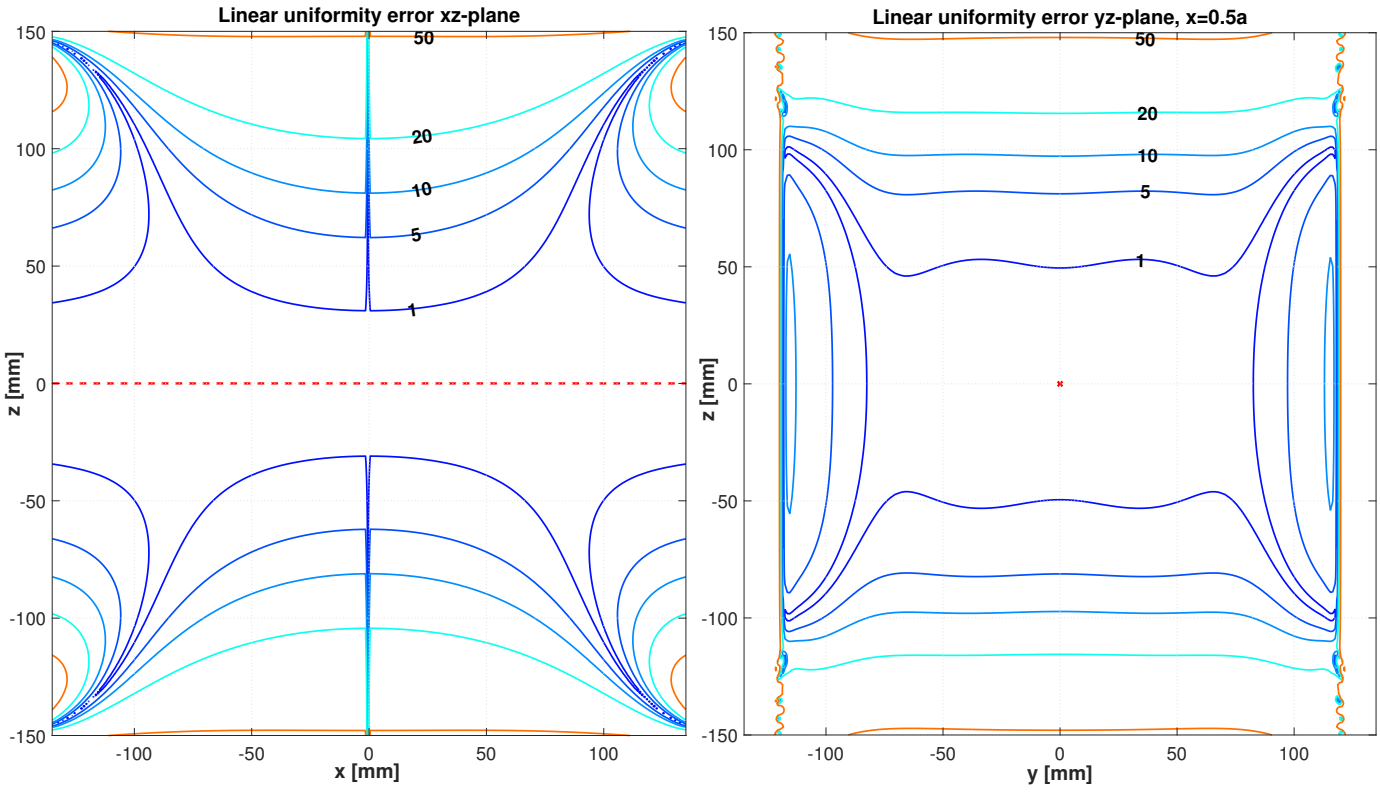

Figure A.4: Linear uniformity error plots of the x-gradient coil. Left corresponds to the xz-plane, right to the yz-plane at x=0.5a.

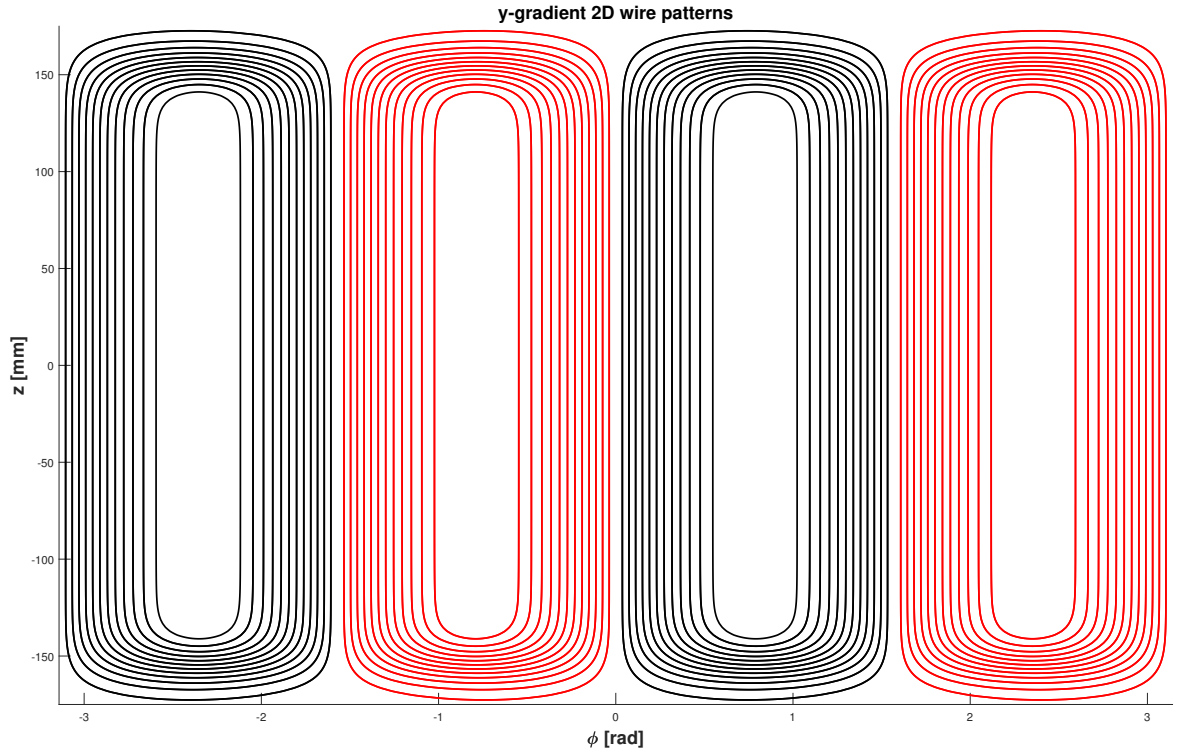

Figure A.5: Two dimensional view of the wire patterns for the y-gradient coil. Red contours correspond to a clockwise direction. Black contours the counterclockwise direction direction.

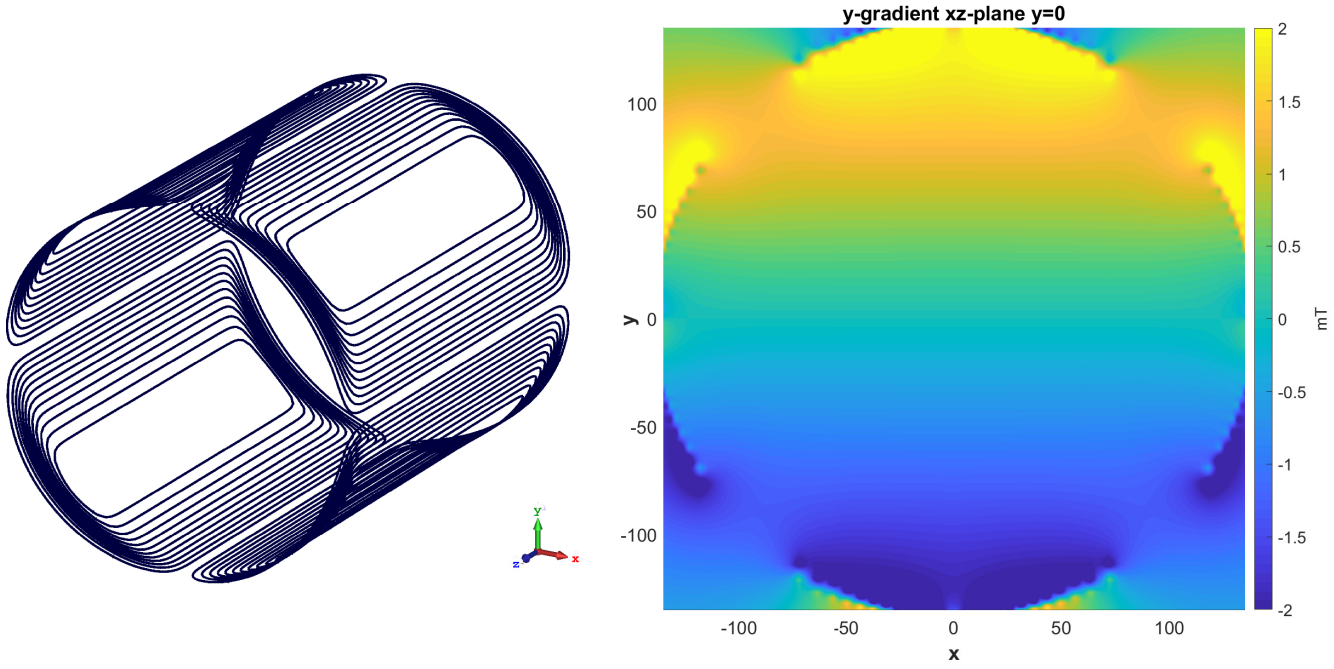

Figure A.6: Left 3D pattern of the y-gradient coil. Right the xy-plane surface plot.

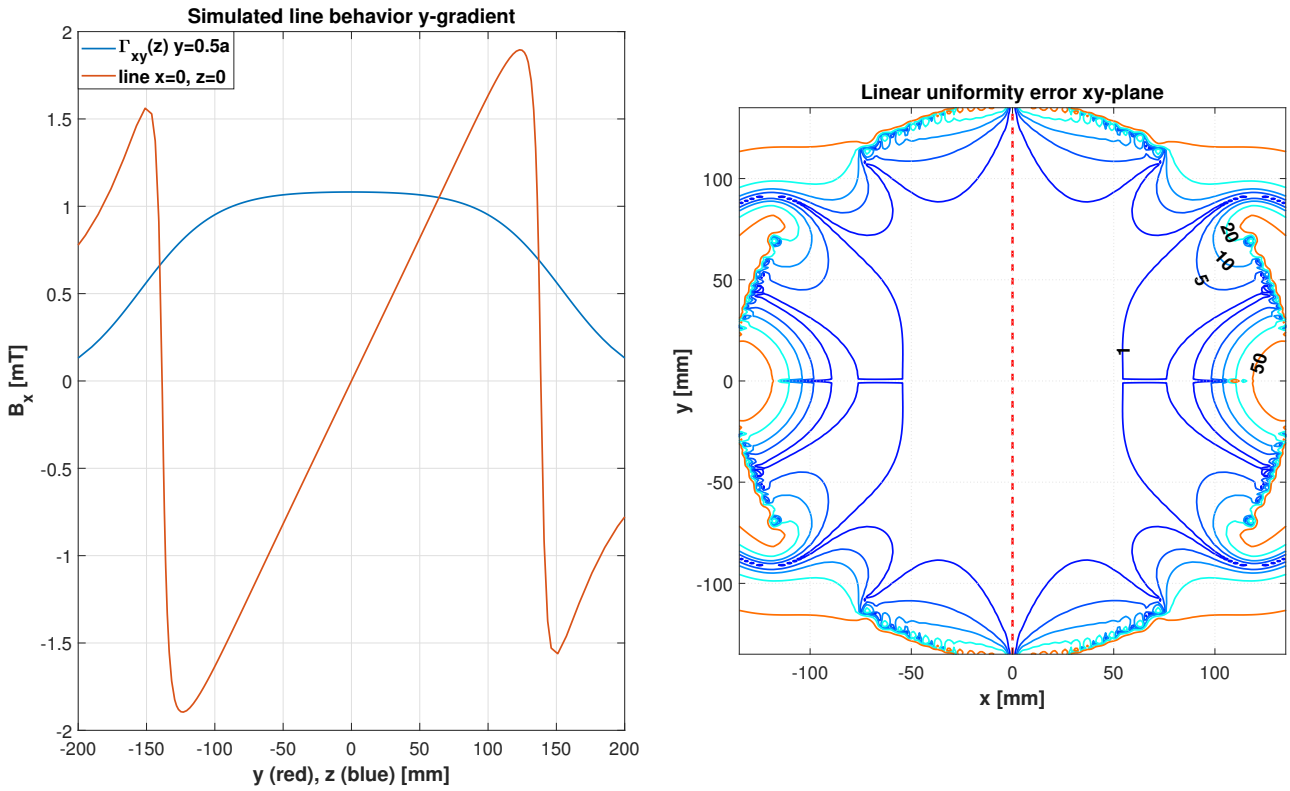

Figure A.7: left figure shows two lines, red shows the linear behavior when taking values on a the red dotted line shown in the right figure. The blue line shows the behavior along the bore axis. This gradient coil is fed with 20[A]. The right figure shows the linear uniformity error plot of the xy-plane.

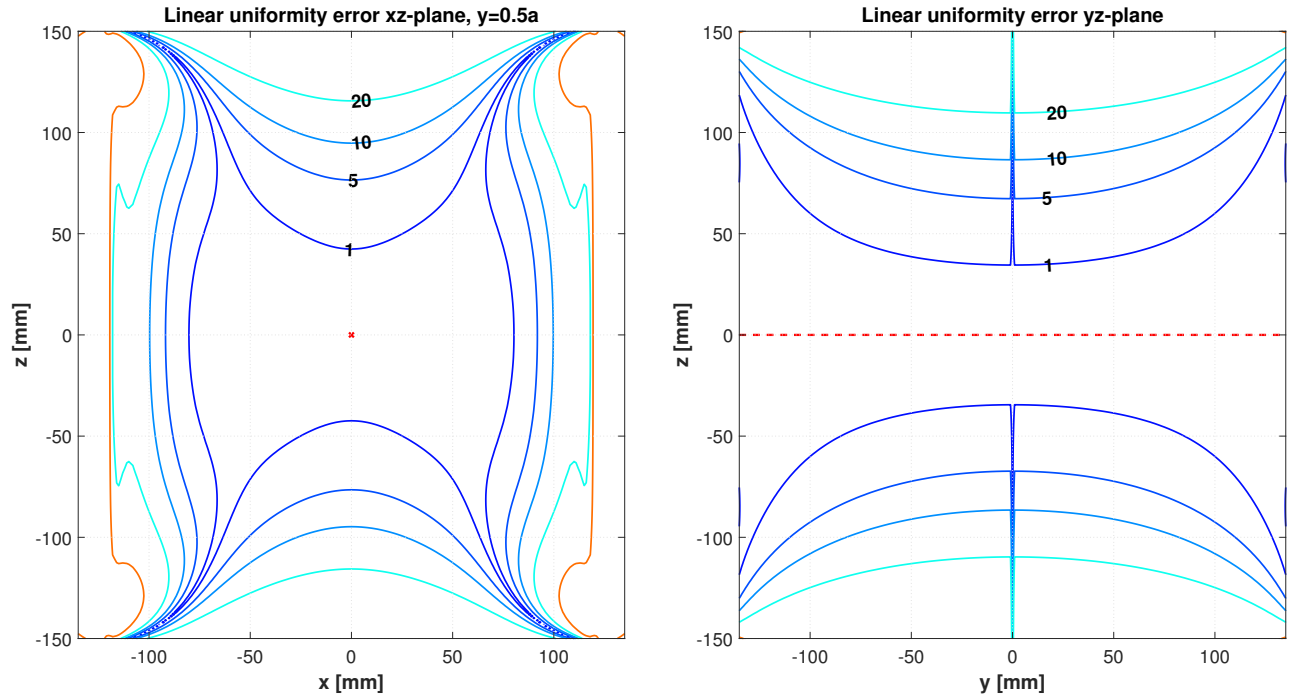

Figure A.8: Linear uniformity error plots of the y-gradient coil. Left corresponds to the xz-plane at y=0.5a, right to the yz-plane. The error was taken with respect to the red dotted lines.

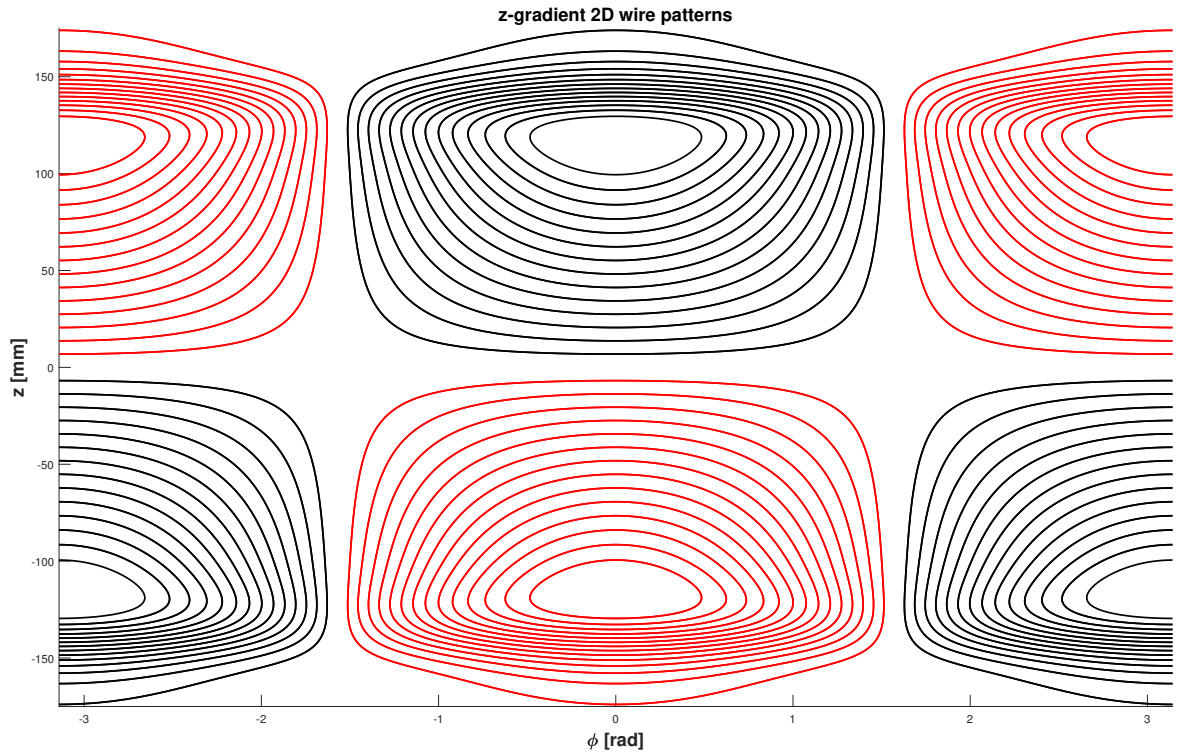

Figure A.9: Two dimensional view of the wire patterns for the z-gradient coil. Red contours correspond to a clockwise direction. Black contours the counterclockwise direction direction.

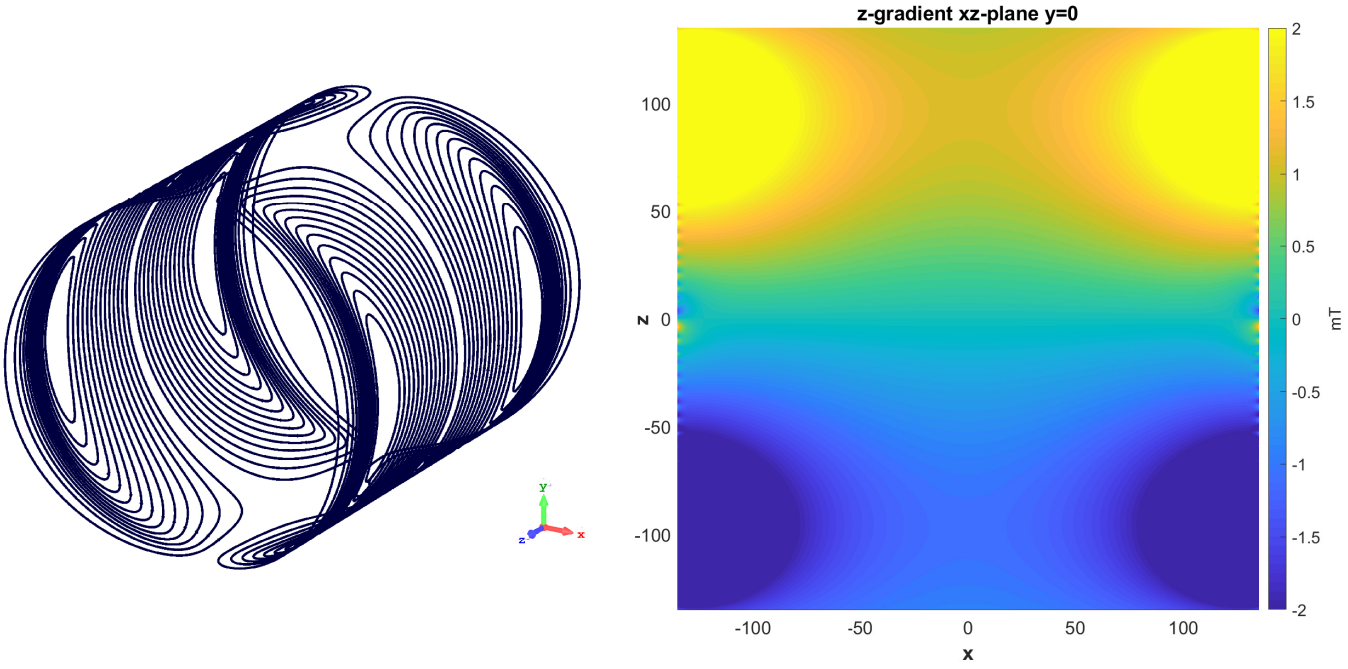

Figure A.10: Left 3D pattern of the z-gradient coil. Right the xz-plane surface plot.

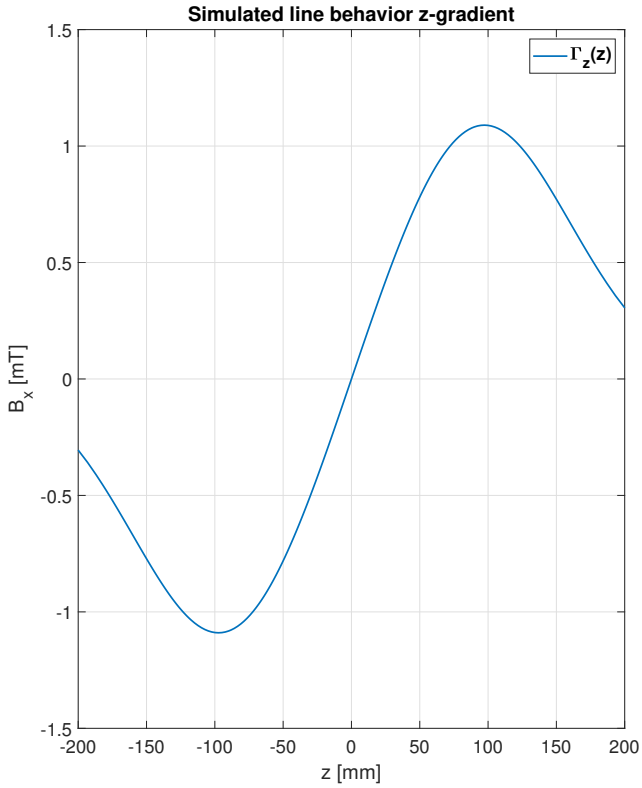

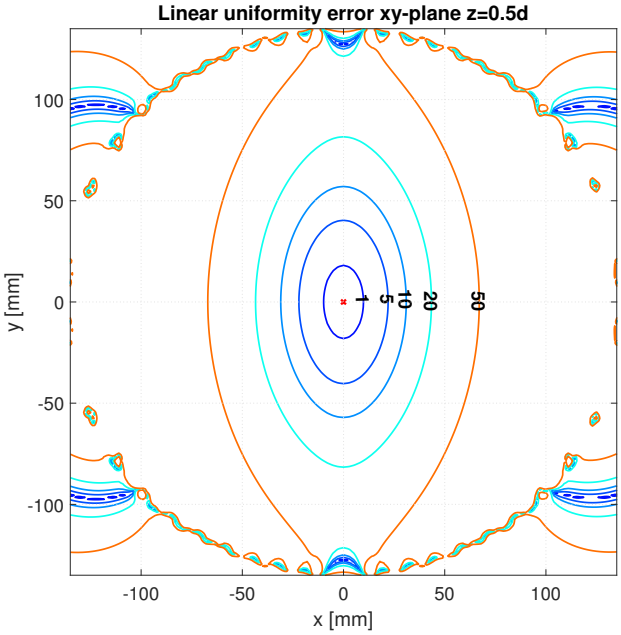

Figure A.11: Left figures shows the linear behavior when taking the values at the middle of the coil along the axis of the bore. This gradient coil is fed with 30[A]. The right figure shows the linear uniformity error of the xy-plane.

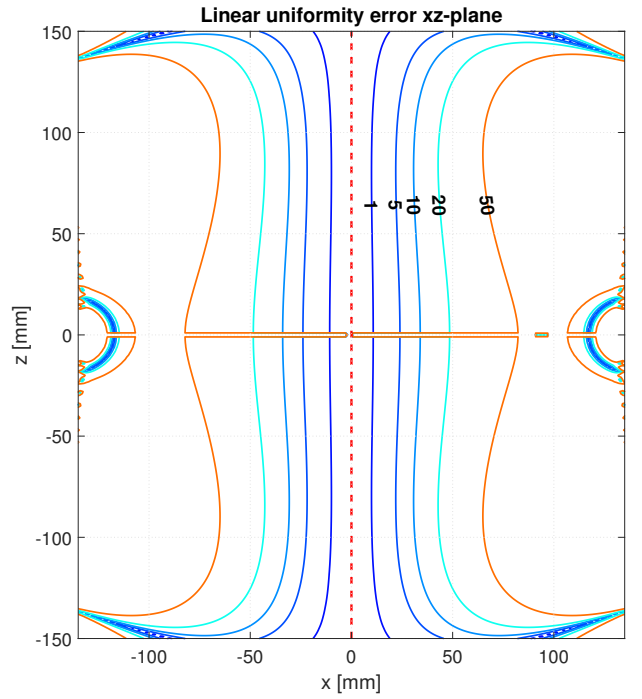

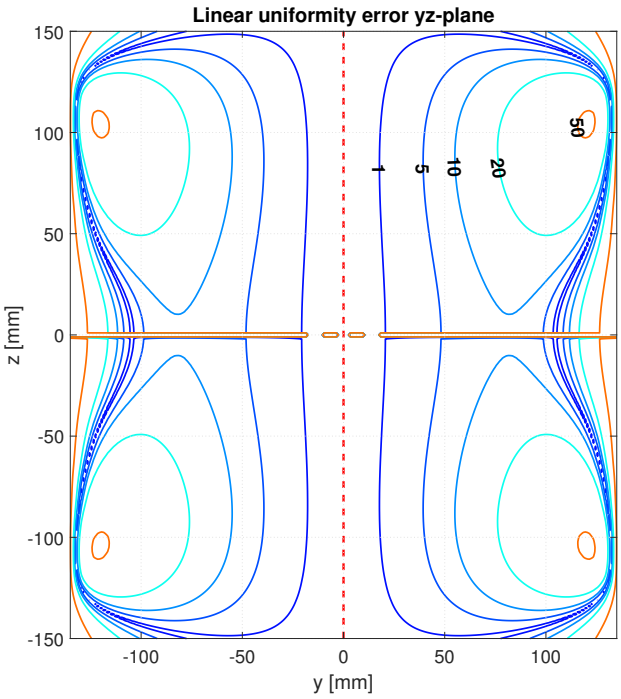

Figure A.12: Linear uniformity error plots of the z-gradient coil. Left corresponds to the xz-plane, right to the yz-plane. The error was taken with respect to the red dotted lines.

BIBLIOGRAPHY

[1] the international federation for Spina Bifida and Hydrocephalus, "facts and figures." https://ifglobal.org/en/what-we-do/global-prevention/prevention-hydrocephalus.

[2] hydrocephalus association, "Symptoms and diagnosis for hydrocephalus." https://hydroassoc.org/symptoms-and-diagnosis.

[3] world health organization, "Global health observatory data repository | by category | medical equipment - data by country." http://apps.who.int/gho/data/view.main.302010.

[4] seattle children's hospital, "Mri brain scan with hydrocephalus." https://seattlechildrens.org/conditions/brain-nervous-system-mental-conditions/hydrocephalus.

[5] F. Vos, "Medical imaging signals and systems." Class notes, Delft University of Technology, 2018.

[6] P. Volegov, J. Mosher, M. Espy, and R. Kraus, "On concomitant gradients in low-field mri," *Journal of Magnetic Resonance*, vol. 175, no. 1, p. 103–113, 2005.

[7] J. O. Nieminen and R. J. Ilmoniemi, "Solving the problem of concomitant gradients in ultra-low-field mri," *Journal of Magnetic Resonance*, vol. 207, no. 2, p. 213–219, 2010.

[8] C. Haacke, *Magnetic resonance imaging: physical principles and sequence design*. Wiley-Liss, 1999.

[9] A. Webb, *Magnetic resonance technology: hardware and system component design*. Royal Society of Chemistry, 2016.

[10] Q. Liu, *A shielded transverse gradient coil for in vivo NMR*. PhD thesis, 1991.

[11] R. Turner, "A target field approach to optimal coil design," *Journal of Physics D: Applied Physics*, vol. 19, no. 8, 1986.

[12] R. Turner, "Minimum inductance coils," *Journal of Physics E: Scientific Instruments*, vol. 21, pp. 948–952, oct 1988.

[13] J. Jin, *Electromagnetic analysis and design in magnetic resonance imaging*. Taylor & Francis group, 2018.

[14] E. A. Chronik and B. K. Rutt, "Constrained length minimum inductance gradient coil design," *Magnetic Resonance in Medicine*, vol. 39, no. 2, p. 270–278, 1998.

[15] R. Turner, "Gradient coil design: A review of methods," *Magnetic Resonance Imaging*, vol. 11, no. 7, p. 903–920, 1993.

[16] S. Hidalgo-Tobon, "Theory of gradient coil design methods for magnetic resonance imaging," *Concepts in Magnetic Resonance Part A*, vol. 36A, no. 4, pp. 223–242, 2010.

[17] T. O'Reilly, W. Teeuwisse, L. Winter, and A. Webb, "The design of a homogenous large-bore halbach array for low field mri," *ISMRM submission paper*, Nov 2018.

[18] M. Abramowitz and I. A. Stegun, *Handbook of mathematical functions with formulas, graphs, and mathematical tables*. U.S. Dept. of Commerce, National Bureau of Standards, 1972.

[19] J. D. Anderson, *Fundamentals of aerodynamics (In SI Units)*. Tata McGraw Hill Education, 2010.

[20] cst studio suite®, "Visual basic commands platform." http://www.mweda.com/cst/cst2013/vba/vba_macro_language_overview.htm.

[21] open source imaging, "Cosi measure, multi-purpose 3-axis robot with submillimeter resolution for static/dynamic field mapping." http://www.opensourceimaging.org/project/cosi-measure/.

[22] alphalab inc., "Gaussmeter model gm2." https://alphalabinc.com/product/gm2/.